
Article:

Valentino, J., He, L. and Gilbert, M. (2026) Application of discontinuity layout optimization to metal shells and assemblies. International Journal for Numerical Methods in Engineering, 127 (5). e70287. ISSN: 0029-5981

https://doi.org/10.1002/nme.70287

International Journal for Numerical Methods in Engineering

WILEY

RESEARCH ARTICLE OPEN ACCESS

Application of Discontinuity Layout Optimization to Metal Shells and Assemblies

John Valentino[1,2] | Linwei He[2] | Matthew Gilbert[2]†

[1]Faculty for the Built Environment, University of Malta, Malta | [2]School of Mechanical, Aerospace and Civil Engineering, University of Sheffield, UK

Correspondence: Linwei He (linwei.he@sheffield.ac.uk)

Received: 30 September 2025 | **Revised:** 25 January 2026 | **Accepted:** 3 February 2026

Keywords: assemblies | connections | discontinuity layout optimization | limit analysis | plasticity | steel

ABSTRACT

Discontinuity Layout Optimization (DLO) provides a computationally efficient means of determining collapse loads and associated failure mechanisms across a wide spectrum of plasticity problems. The classical DLO method has focused separately on in-plane and out-of-plane plasticity. In the present work, the method is extended to thin-walled shell structures, where the interactions between in-plane and out-of-plane forces and moments are captured through both surface and point contact formulations. To assess the efficacy and generality of the approach, a series of benchmark problems are investigated, including metal sections, cylindrical and spherical shells, T-stub, end-plate connections and assemblies. The results are evaluated against theoretical equations, established numerical benchmarks from the literature and Eurocode standards, thereby demonstrating both the accuracy and practical relevance of the proposed formulations.

1 | Introduction

The classical theory of plasticity emerged from the study of metals in the late nineteenth century and concerns materials that initially deform elastically but undergo plastic deformation once a yield stress is reached. Plasticity theory began with Tresca in 1864, when he undertook an experimental program into the extrusion of metals and published his famous yield criterion [1]. Further advances with yield criteria and plastic flow rules were made in the years which followed by Saint-Venant, Levy, Von Mises, Hencky and Prandtl. The 1940s saw the advent of the classical theory; Prager, Hill, Drucker and Koiter amongst others brought together many fundamental aspects of the theory [2].

Finite element analysis (FEA) has been used in the research of steel connections in recent decades, together with element-free Galerkin (EFG) meshless methods. In the interests of speed and to limit the amount of data that needs to be handled, shell elements rather than solid elements have proved popular, together with analysis methods that cater

---

†Deceased.

for geometric and material non-linearity [3]. Prior to these solutions were obtained from physical laboratory testing or from analytical closed-form solutions, based on general yield line theory by Ingerslev, Johansen and Gvozdev for concrete slabs, also applied to metals [4, 5]. Computational methods capable of explicitly identifying yield-lines were also developed [6–8]; these methods are similar, each placing potential yield-lines at the boundaries of rigid elements arranged in a finite element mesh.

Discontinuity layout optimization (DLO) is a numerical analysis optimization procedure for continuum mechanics that determines the failure mechanism based on specified failure criteria. The procedure discretizes the continuum into a number of potential discontinuities that can overlap or crossover one another. The advantage over previously proposed methods [7, 9, 10] is that potential discontinuities, which interlink nodes laid out over the body under consideration, are permitted to crossover one another, giving a much wider search space than when such discontinuities are located on the boundaries of rigid triangular elements with a fixed topology. Highly efficient interior point and conic programming solvers can be employed to solve the underlying mathematical problem. This procedure is related to that used to identify the optimal layout of bars in 'Michell' trusses, first proposed by Dorn et al. [11], with slip-line discontinuities in a translational failure mechanism corresponding to bars in an optimum truss. DLO has been used in the analysis of a range of geotechnical engineering problems (e.g., slope stability, bearing capacity and retaining wall problems), concrete slab problems and metal forming or extrusion problems. In particular, the procedure has been used to determine the critical layout of discontinuities and the associated upper-bound limit load for in-plane and out-of-plane plasticity problems [12, 13]. A time dependent stability analysis for concrete tunnel lining using DLO was carried out by Sun et al. [14]. DLO has also been applied to 3D solid plasticity problems by Hawksbee et al. [15] and Zhang [16], where a surface discontinuity formulation involving polygonal discontinuities was used, with second-order cone programming techniques used to successfully solve a series of simple benchmark problems.

Several techniques have been developed to increase solution speed and/or to refine the solutions obtainable via DLO. A technique first developed for truss optimization problems is the 'member adding' procedure [17], which makes use of the duality property of linear programming. In this technique, an initial result is sought using an initial minimally connected ground structure in which each node is connected only to its neighbours (by a potential truss bar or, in this case, by a potential discontinuity). The result is iteratively improved by checking if constraints in the dual problem are violated, with additional connections added to the ground structure if this is the case. Also, a geometry optimization formulation can be used, in which the positions of nodes are now design variables to improve the solutions used [18]. In this case an initial solution is obtained as normal using a fixed grid of nodes, with the geometry optimization step then applied. Also, the yield criteria can be adaptively improved, as proposed by Smith and Gilbert [19]. Zhang et al. [20] has also introduced a virtual displacement based discontinuity layout optimization that takes the stress state of a loaded structure as a snapshot and correspondingly provides the optimum failure pattern. In relation to yield criteria, several authors have proposed yield criteria for shells and plates, including Save and Massonnet [21] and Nielsen and Hoang [22]. With DLO one may wish to identify the rigid solids formed after solution of the optimization problem; in this case convex hull search criteria formulations used with Delaunay triangulation have been employed by Shalloway and Trott [23], De Berg et al. [24] and Hua [25], though these formulations are more difficult to implement in 3D than 2D.

Timmers [26] studied the in-plane behaviour of steel plates with notches, holes, and bolts using DLO. The bolts were not modelled explicitly; instead, the edges of the bolt holes were fixed to approximately represent the bolts. Timmers [27] also used 2D DLO to study the out-of-plane behaviour of stiffened and unstiffened T-stubs. In the out-of-plane models a number of boundary conditions were imposed to simulate compression only in bearing to allow lift off and/or fixed rotation on the stiff member of the stub. He et al. [28] studied a number of boundary conditions that can be formulated in DLO for slabs or plates. When analysing steel connections, the 'component method' is often used, in which the connection is divided into individual components, verified against the resistance of components listed in [29], where the latter make use of the theorems of plasticity. Thus Timmers [26, 27] studied single steel components using 2D DLO for in-plane or out-of-plane problems and later extended the research to include bolts and T-stubs.

Although 3D DLO methods have been developed, their computational cost remains high. Consequently, an efficient formulation specifically tailored to thin-walled 3D shell structures is required. Key challenges include the efficient representation of discontinuities along curved shell geometries, the enforcement of compatibility conditions between discontinuities in a 3D setting, and the treatment of coupling effects between in-plane and out-of-plane displacement jumps. This paper addresses these challenges, with particular emphasis on applications to metal connections and structural assemblies. The sturcture of the paper is as follows: in Section 2 details of a new shell DLO formulation is presented; in Section 3

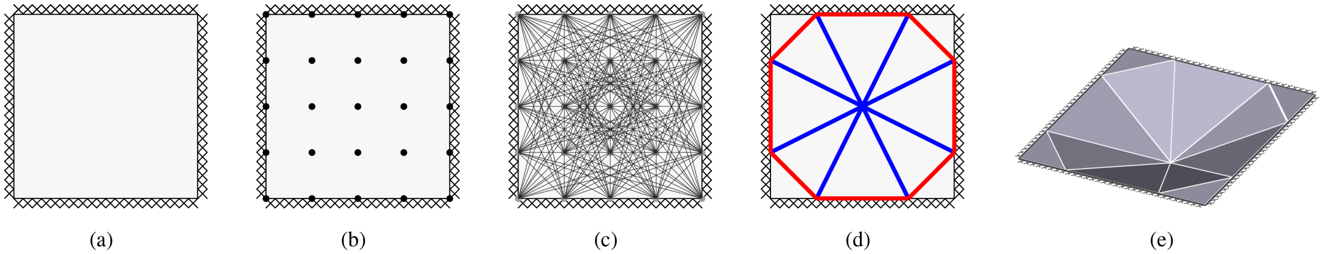
(a) (b) (c) (d) (e)

FIGURE 1 | Steps in the DLO process (for a fixed-supported square slab under out-of-plane loading): (a) problem definition; (b) nodal discretization; (c) generation of potential discontinuities by interconnecting all nodes; (d) identification of the subset of discontinuities corresponding to the critical collapse mechanism via optimization; (e) visualization of the deformed shape.

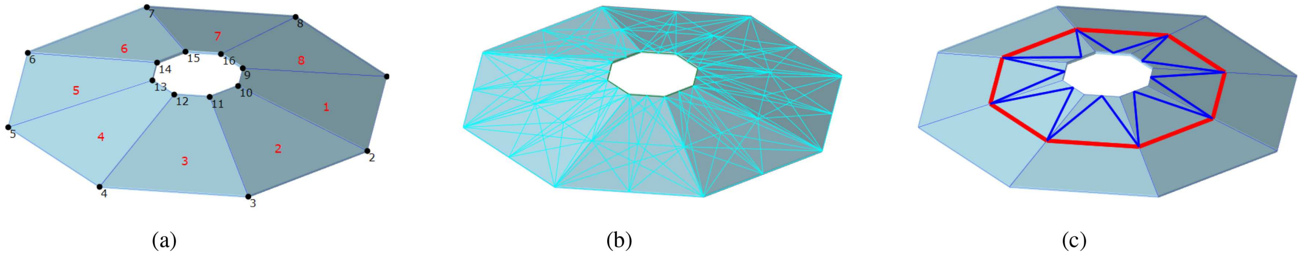

(a) (b) (c)

FIGURE 2 | Shell DLO via piecewise-linear planar approximation: (a) geometry of problem, comprising a series of 8 planar sub-domains; (b) potential discontinuities within each sub-domain; (c) critical subset of discontinuities defining the failure mechanism, identified via optimization.

details of applicable yield criteria are presented and point and surface contact formulations are described; in Section 4 a range of examples are used to allow the DLO solutions to be compared with literature solutions; examples include a metal assembly made of different components. Finally, conclusions are drawn in Section 5.

2 | Discontinuity Layout Optimization

DLO relies on the upper bound theorem of plasticity theory, using work equations and equating the internal and external work done on the system. The classical DLO method involves five steps, as illustrated in Figure 1. First, the problem domain is defined. Nodes are then generated within the domain, followed by the creation of potential discontinuities by interconnecting all nodes. The resulting set of discontinuities typically represents an extremely large number of potential failure mechanisms. An optimization problem is subsequently solved to identify the subset of discontinuities corresponding to the most critical collapse mechanism. Finally, the deformed shape can be visualized to aid interpretation.

For 3D shell structures, a piecewise-linear planar approximation is employed, in which the 3D shell domain is represented by multiple planar sub-domains, as illustrated in Figure 2. Although the core DLO steps remain the same, and separate in-plane and out-of-plane methods have been developed [13, 19], substantial modifications are required to combine them into a 3D shell DLO formulation, due to the increased geometric complexity and the coupling between forces and moments.

2.1 | Notation

The notation used in the contribution for a displacement jump across a discontinuity is represented in Figure 3. Superscripts 1 & 2 represent the two ends of the discontinuity and subscripts 1, 2 & 3 represent the three local directions with displacement jumps δ or equivalent forces f, and rotation jumps θ or equivalent moments m, whereas x, y, z represent the three global directions. The local displacement vector is defined as $\boldsymbol{\delta}$ and the global displacement vector as $\boldsymbol{\Delta}$. With this notation the shear directions are 1 & 3 and the normal direction 2. A kinematic or static problem formulation may be employed; the former is adopted here.

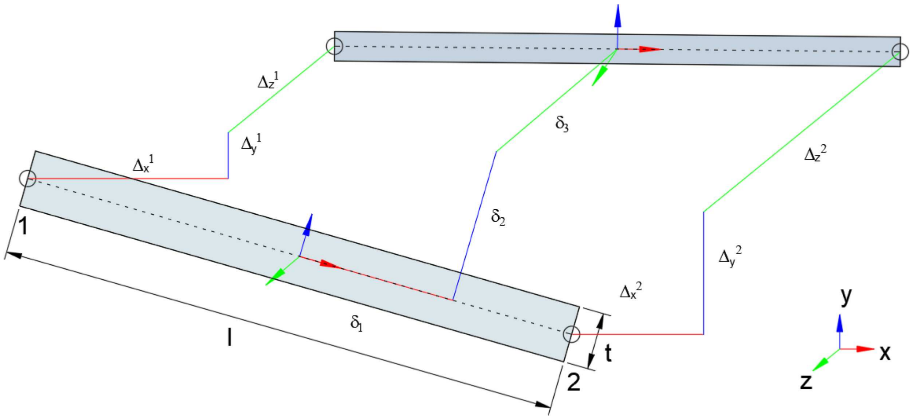

FIGURE 3 | Discontinuity at sub-domain boundary with deformations notation in local and global axis.

2.2 | Compatibility Matrix

The compatibility matrix ensures that the sum of the relative displacement jumps at the end of each discontinuity is equal to zero. The transformation matrix **T** relating the displacement jumps at the centre of the discontinuity i to the end of a given sub-domain can be written as $\boldsymbol{\delta} = \mathbf{Td}$. The rotation matrix **R** transforming the local axis to the global axis can be written as $\boldsymbol{\Delta} = \mathbf{R}\boldsymbol{\delta}$, where,

$$\mathbf{R} = \begin{bmatrix} \mathbf{r} & \mathbf{0} & \mathbf{0} & \mathbf{0} \\ \mathbf{0} & \mathbf{r} & \mathbf{0} & \mathbf{0} \\ \mathbf{0} & \mathbf{0} & \mathbf{r} & \mathbf{0} \\ \mathbf{0} & \mathbf{0} & \mathbf{0} & \mathbf{r} \end{bmatrix}, \quad \mathbf{r} = \begin{bmatrix} l_\mathrm{x} & l_\mathrm{y} & l_\mathrm{z} \\ m_\mathrm{x} & m_\mathrm{y} & m_\mathrm{z} \\ n_\mathrm{x} & n_\mathrm{y} & n_\mathrm{z} \end{bmatrix} \tag{1}$$

and l_x, l_y, l_z, m_x, m_y, m_z, n_x, n_y and n_z are direction cosines. The global axis vector of displacements $\boldsymbol{\Delta}$ at the far end of discontinuity i can be written in terms of the local axis vector $\boldsymbol{\delta}$ and the compatibility matrix **B**, such that $\boldsymbol{\Delta} = \mathbf{Bd}$. The compatibility matrix **B** equates to $\mathbf{B} = \mathbf{RT}$, where **d** represent the displacements in the local axes 1, 2, 3 at the middle of the discontinuity line, $\boldsymbol{\delta}$ represent the displacements in the local axes 1, 2, 3 at ends 1 and 2 of the discontinuity line, $\boldsymbol{\Delta}$ represents displacements in the x, y, z global axes at ends 1 and 2 of the discontinuity line. Compatibility at a node considering translation only is illustrated in Figure 4.

$$\mathbf{T} = \begin{bmatrix} 1 & 0 & 0 & 0 & 0 & 0 \\ 0 & 1 & 0 & 0 & 0 & \frac{l}{2} \\ 0 & 0 & 1 & 0 & -\frac{l}{2} & 0 \\ 0 & 0 & 0 & 1 & 0 & 0 \\ 0 & 0 & 0 & 0 & 1 & 0 \\ 0 & 0 & 0 & 0 & 0 & 1 \\ -1 & 0 & 0 & 0 & 0 & 0 \\ 0 & -1 & 0 & 0 & 0 & \frac{l}{2} \\ 0 & 0 & -1 & 0 & -\frac{l}{2} & 0 \\ 0 & 0 & 0 & -1 & 0 & 0 \\ 0 & 0 & 0 & 0 & -1 & 0 \\ 0 & 0 & 0 & 0 & 0 & -1 \end{bmatrix}, \quad \mathbf{B} = \begin{bmatrix} l_\mathrm{x} & l_\mathrm{y} & l_\mathrm{z} & 0 & -\frac{l_\mathrm{z} l}{2} & \frac{l_\mathrm{y} l}{2} \\ m_\mathrm{x} & m_\mathrm{y} & m_\mathrm{z} & 0 & -\frac{m_\mathrm{z} l}{2} & \frac{m_\mathrm{y} l}{2} \\ n_\mathrm{x} & n_\mathrm{y} & n_\mathrm{z} & 0 & -\frac{n_\mathrm{z} l}{2} & \frac{n_\mathrm{y} l}{2} \\ 0 & 0 & 0 & l_\mathrm{x} & l_\mathrm{y} & l_\mathrm{z} \\ 0 & 0 & 0 & m_\mathrm{x} & m_\mathrm{y} & m_\mathrm{z} \\ 0 & 0 & 0 & n_\mathrm{x} & n_\mathrm{y} & n_\mathrm{z} \\ -l_\mathrm{x} & -l_\mathrm{y} & -l_\mathrm{z} & 0 & -\frac{l_\mathrm{z} l}{2} & \frac{l_\mathrm{y} l}{2} \\ -m_\mathrm{x} & -m_\mathrm{y} & -m_\mathrm{z} & 0 & -\frac{m_\mathrm{z} l}{2} & \frac{m_\mathrm{y} l}{2} \\ -n_\mathrm{x} & -n_\mathrm{y} & -n_\mathrm{z} & 0 & -\frac{n_\mathrm{z} l}{2} & \frac{n_\mathrm{y} l}{2} \\ 0 & 0 & 0 & -l_\mathrm{x} & -l_\mathrm{y} & -l_\mathrm{z} \\ 0 & 0 & 0 & -m_\mathrm{x} & -m_\mathrm{y} & -m_\mathrm{z} \\ 0 & 0 & 0 & -n_\mathrm{x} & -n_\mathrm{y} & -n_\mathrm{z} \end{bmatrix} \tag{2}$$

$$\mathbf{d} = \begin{bmatrix} \delta_1 & \delta_2 & \delta_3 & \theta_1 & \theta_2 & \theta_3 \end{bmatrix}^\mathrm{T} \tag{3}$$

$$\boldsymbol{\Delta} = \begin{bmatrix} \delta_\mathrm{x}^1 & \delta_\mathrm{y}^1 & \delta_\mathrm{z}^1 & \theta_\mathrm{x}^1 & \theta_\mathrm{y}^1 & \theta_\mathrm{z}^1 & \delta_\mathrm{x}^2 & \delta_\mathrm{y}^2 & \delta_\mathrm{z}^2 & \theta_\mathrm{x}^2 & \theta_\mathrm{y}^2 & \theta_\mathrm{z}^2 \end{bmatrix}^\mathrm{T} \tag{4}$$

$$\boldsymbol{\delta} = \begin{bmatrix} \delta_1^1 & \delta_2^1 & \delta_3^1 & \theta_1^1 & \theta_2^1 & \theta_3^1 & \delta_1^2 & \delta_2^2 & \delta_3^2 & \theta_1^2 & \theta_2^2 & \theta_3^2 \end{bmatrix}^\mathrm{T} \tag{5}$$

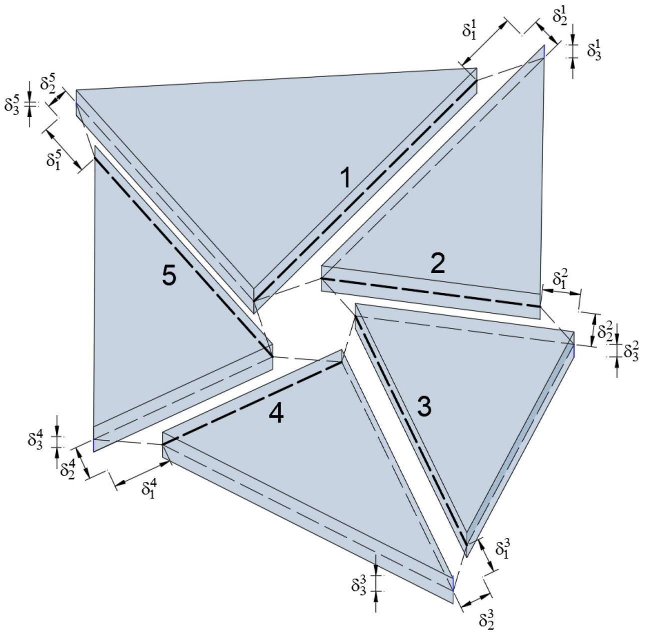

FIGURE 4 | Compatibility of translational displacement jumps at a node with five discontinuities.

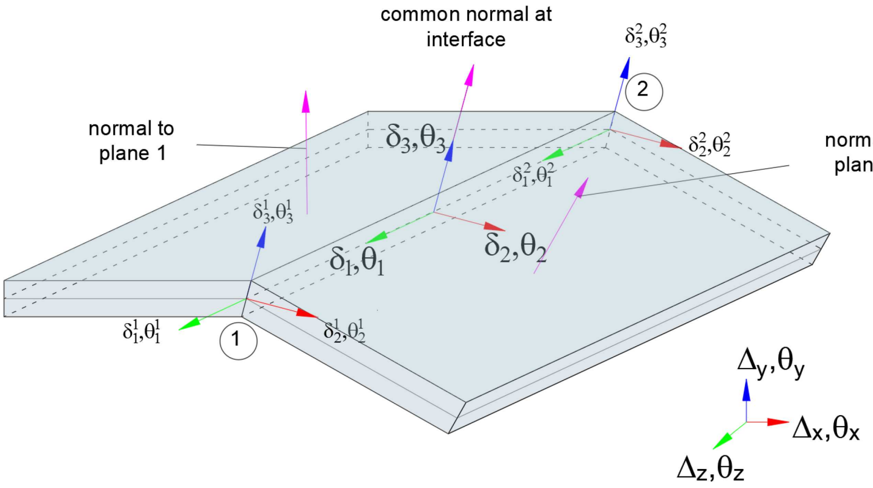

FIGURE 5 | Discontinuity at a sub-domain boundary.

2.3 | Discontinuity Along Sub-Domain Boundary

The discontinuity along the boundary of two adjacent sub-domains may have different normal directions and thickness, as indicated in Figure 5. A smeared thickness and normal can be calculated for these discontinuities. The normal $\hat{n}_\mathrm{i}$ at an intersection may be written as:

$$\hat{n}_\mathrm{i} = n_\mathrm{i,x}, n_\mathrm{i,y}, n_\mathrm{i,z} = \frac{n_\mathrm{1,x} + n_\mathrm{2,x}, n_\mathrm{1,y} + n_\mathrm{2,y}, n_\mathrm{1,z} + n_\mathrm{2,z}}{\sqrt{(n_\mathrm{1,x} + n_\mathrm{2,x})^2 + (n_\mathrm{1,y} + n_\mathrm{2,y})^2 + (n_\mathrm{1,z} + n_\mathrm{2,z})^2}} \tag{6}$$

and the smeared thickness t_i for adjacent elements with the same thickness t_1 and t_2 as:

$$t_\mathrm{i} = \frac{t_1}{\sqrt{\dfrac{n_\mathrm{1,x}n_\mathrm{2,x} + n_\mathrm{1,y}n_\mathrm{2,y} + n_\mathrm{1,z}n_\mathrm{2,z} + 1}{2}}} \tag{7}$$

where $\hat{n}_1$ and $\hat{n}_2$ are the unit normal vectors of plane 1 and plane 2 respectively, $\hat{n}_\text{i}$ is the common normal, t_1 and t_2 are the thicknesses of the respective sub-domains and t_i is the thickness at the interface. The normal direction can be rotated to lie in the horizontal direction so as to model horizontal supports.

2.4 | Kinematic DLO Formulation

The DLO procedure is posed as an optimization problem. In the kinematic formulation the objective function is to minimize the internal work done along the yield lines. The failure load is determined from the upper bound theorem and plasticity theory by using the work equations and equating the internal and external work done on the system. The work balance equation and can be stated as (after Smith and Gilbert [12]):

$$\min \quad \lambda \mathbf{f}_\text{L}^\text{T}\mathbf{d} = -\mathbf{f}_\text{D}^\text{T}\mathbf{d} + \mathbf{g}^\text{T}\mathbf{p} \tag{8}$$

subject to:

$$\begin{aligned} \mathbf{Bd} &= 0 \\ \mathbf{Np} - \mathbf{d} &= 0 \\ \mathbf{f}_\text{L}^\text{T}\,\mathbf{d} &= 1 \\ \mathbf{p} &\geq 0 \end{aligned} \tag{9}$$

where λ is a dimensionless load (or 'adequacy') factor, **d** is a vector containing the displacement and rotation jumps along discontinuities, **p** is a vector of plastic multipliers, $\mathbf{f}_\text{D}$ and $\mathbf{f}_\text{L}$ are vectors prescribing dead and live load effects, respectively, evaluated within each sub-domain via classical DLO approaches [12, 13]. **B** is the aforementioned compatibility matrix. **N** is the plastic flow matrix and **g** is a vector of dissipation coefficients; both depend on the selected yield criteria. The formulation accommodates various boundary conditions, including free, simply supported, or fixed supports, lines of symmetry, as well as specific displacement constraints, such as compression-only contact, as illustrated in He et al. [28].

3 | Yield Criteria

Here the focus will be on applying DLO to steel components and assemblies. Different yield criteria can be adopted for different components of an assembly, i.e., for a metal plate, bolt or weld.

3.1 | Metal Plates

For metal steel plates two independent yield criteria are considered: one that models interaction between axial force and moment; one that models interaction between shear and axial force. In this study an isotropic material without any strain hardening is assumed for a metal of yield stress f_y.

3.1.1 | Moment and Axial Force Interaction

In its simplest form the moment vs axial force yield surface for metals can be expressed as in Figure 6a, without any interaction between moment and axial force as in Wong [30]. This simple square yield surface can be expressed as:

$$|m^*| \leq 1; \quad |n^*| \leq 1; \tag{10}$$

where m^* and n^* are normalized moment and axial force respectively, defined using

$$m^* = \begin{cases} \dfrac{M_{1,\text{Ed}}}{M_{1,\text{Rd}}}, & \text{(out-of-plane)} \\ \dfrac{M_{3,\text{Ed}}}{M_{3,\text{Rd}}}, & \text{(in-plane)} \end{cases} \tag{11}$$

$$n^* = \frac{F_{2,\text{Ed}}}{F_{2,\text{Rd}}}, \tag{12}$$

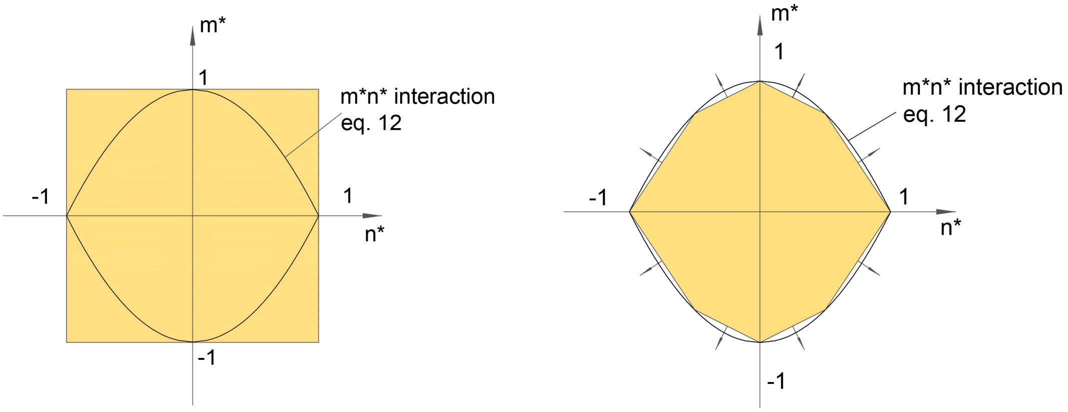

(a) (b)

FIGURE 6 | Normalized moment vs axial force yield surfaces: (a) no interaction case (Equation 10); (b) with linearized M-N interaction (Equation 14). The standard 'with interaction' case (Equation 13) is also shown in (a) and (b).

where $M_{1,\mathrm{Ed}}$ is out-of-plane moment, and $M_{1,\mathrm{Rd}} = f_{\mathrm{y}}\frac{lt^2}{4}$ denotes its limiting value (i.e., the plastic moment capacity), with f_{y} being the material yield stress, and t and length l representing the thickness and length of the discontinuity interface, respectively. Similarly, $M_{3,\mathrm{Ed}}$ and $M_{3,\mathrm{Rd}} = f_{\mathrm{y}}\frac{tl^2}{4}$ are the in-plane moment and its limiting value, respectively. $F_{2,\mathrm{Ed}}$ and $F_{2,\mathrm{Rd}} = f_{\mathrm{y}}lt$ represent the normal forces and its limiting value, respectively.

A more refined moment vs axial force yield surface that considers reduction of membrane force capacity with applied moment was derived by Save and Massonnet [21] as follows:

$$|m^*| + n^{*2} - 1 \leq 0 \tag{13}$$

The yield surface can be expressed as eight separate yield constraints by dividing the surface into eight linear segments. These yield surfaces are represented in Figure 6b. The eight linearized conditions can be written as:

$$\begin{bmatrix} \mathbf{A}_1 \\ \mathbf{A}_2 \\ \mathbf{A}_3 \end{bmatrix}^{\mathrm{T}} \begin{bmatrix} n^* \\ m^* \\ -1 \end{bmatrix} \leq 0, \tag{14}$$

where

$$\begin{aligned} \mathbf{A}_1 &= \begin{bmatrix} 1 & 1 & -1 & -1 & 3 & 3 & -3 & -3 \end{bmatrix}, \\ \mathbf{A}_2 &= \begin{bmatrix} 2 & -2 & 2 & -2 & 2 & -2 & 2 & -2 \end{bmatrix}, \\ \mathbf{A}_3 &= \begin{bmatrix} 2 & 2 & 2 & 2 & 3 & 3 & 3 & 3 \end{bmatrix}, \end{aligned} \tag{15}$$

are the coefficient matrices for the linear approximation. Substitute m^* and n^* with the expressions given in Equations (11) and (12) and remove redundant constraints:

$$\begin{bmatrix} \mathbf{A}_1 \\ \frac{4}{t}\mathbf{A}_2 \end{bmatrix}^{\mathrm{T}} \begin{bmatrix} F_{2,\mathrm{Ed}} \\ M_{1,\mathrm{Ed}} \end{bmatrix} \leq 0; \quad \begin{bmatrix} \mathbf{A}_1 \\ \frac{4}{l}\mathbf{A}_2 \end{bmatrix}^{\mathrm{T}} \begin{bmatrix} F_{2,\mathrm{Ed}} \\ M_{3,\mathrm{Ed}} \end{bmatrix} \leq 0 \tag{16}$$

which describes the yield criterion in terms of forces and moments acting along the discontinuity interfaces. Based on normality rule, the flow rule matrix for displacement variables δ_2, θ_1, and θ_3 can be derived as:

$$\begin{bmatrix} \mathbf{A}_1 \\ \frac{4}{t}\mathbf{A}_2 \end{bmatrix} \begin{bmatrix} p_1 \\ \vdots \\ p_8 \end{bmatrix} - \begin{bmatrix} \delta_2 \\ \theta_1 \end{bmatrix} = 0; \quad \begin{bmatrix} \mathbf{A}_1 \\ \frac{4}{l}\mathbf{A}_2 \end{bmatrix} \begin{bmatrix} p_9 \\ \vdots \\ p_{16} \end{bmatrix} - \begin{bmatrix} \delta_2 \\ \theta_3 \end{bmatrix} = 0$$

which can be combined as:

$$\mathbf{Np} - \mathbf{d} = \mathbf{N}\begin{bmatrix} p_1 \\ \vdots \\ p_{16} \end{bmatrix} - \begin{bmatrix} \delta_2 \\ \theta_1 \\ \theta_3 \end{bmatrix} = 0;\ \text{where } \mathbf{N} = \begin{bmatrix} \mathbf{A}_1 & \mathbf{A}_1 \\ \frac{4}{t}\mathbf{A}_2 & 0 \\ 0 & \frac{4}{l}\mathbf{A}_2 \end{bmatrix} \tag{17}$$

where $p_1, p_2, \dots, p_{16} \geq 0$ are plastic multipliers. And the work equation can be derived as:

$$\mathbf{g}^{\mathrm{T}} = f_{\mathrm{y}} lt \begin{bmatrix} \mathbf{A_3} & \mathbf{A_3} \end{bmatrix} \tag{18}$$

for a discontinuity interface.

3.1.2 | Shear and Axial Force Interaction

The interaction between axial stress σ and shear stress τ may be expressed in its simplest uncoupled form as:

$$\left| \frac{\sigma}{f_{\mathrm{y}}} \right| \leq 1; \quad \left| \frac{\tau}{f_{\mathrm{v}}} \right| \leq 1 \tag{19}$$

where $f_{\mathrm{v}} = f_{\mathrm{y}}/2$ based on Tresca and $f_{\mathrm{v}} = f_{\mathrm{y}}/\sqrt{3}$ based on Von Mises for uniaxial tension or compression.

An improved yield criterion for interaction between axial and shear force for a thin shell element has been developed [21, 31] (see also Appendix B):

$$\left(\frac{\sigma}{f_{\mathrm{y}}} \right)^2 + \left(\frac{\tau}{f_{\mathrm{v}}} \right)^2 \leq 1 \tag{20}$$

In the derivation of this equation, it has been assumed that $\sigma_2 = 0$. This assumption can lead to conservative or non-conservative results, depending on whether σ_2 is beneficial to σ_1 (e.g., when both are in tension or compression) or not beneficial (e.g., when these have opposite signs). This limitation is necessary as the standard DLO formulation only considers direct normal and shear stresses at a discontinuity line.

The yield surface can be expressed either as a conic optimization problem or as an approximated linear optimization problem. The latter approximates the yield surface via eight linear segments shown in Figure 7, written as:

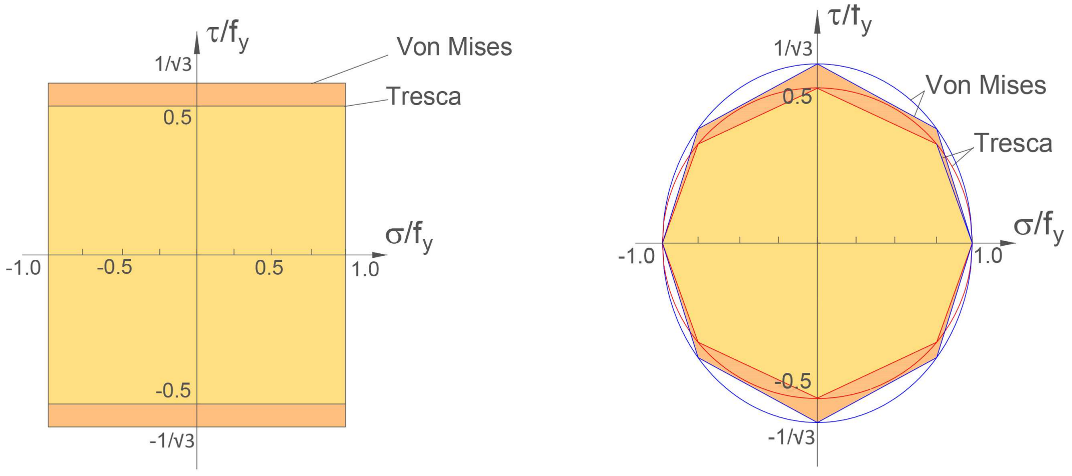

(a)

(b)

FIGURE 7 | Normalized shear vs axial stress yield surfaces: (a) no interaction (simple square V-N criteria), for Von Mises and Tresca criteria (Equation 19); (b) inscribed linearized interaction between normalized shear and axial stress (linearized V-N criteria) for Von Mises and Tresca criteria (Equation 21).

$$\begin{bmatrix}\mathbf{A}_1\\ \mathbf{A}_2\end{bmatrix}^{\mathrm{T}}\begin{bmatrix}\tau\\ \sigma\\ -1\end{bmatrix}\le 0 \tag{21}$$

where:

$$\mathbf{A}_1=\begin{bmatrix}1 & 1 & -1 & -1 & 1 & 1 & -1 & -1\\ k\left(\frac{4-\sqrt{7}}{3}\right) & k\sqrt{7} & k\left(\frac{4-\sqrt{7}}{3}\right) & k\sqrt{7} & k\left(\frac{4-\sqrt{7}}{3}\right) & k\sqrt{7} & k\left(\frac{4-\sqrt{7}}{3}\right) & k\sqrt{7}\end{bmatrix} \tag{22}$$

$$\mathbf{A}_2=\begin{bmatrix}k & k\sqrt{7} & k & k\sqrt{7} & k & k\sqrt{7} & k & k\sqrt{7}\end{bmatrix} \tag{23}$$

where for Tresca criterion $k=1/2$ and for Von Mises $k=1/\sqrt{3}$. The flow matrix in DLO, including also the out-of-plane shear displacement without any interaction, may be written as:

$$\mathbf{Np}-\mathbf{d}=\mathbf{N}\begin{bmatrix}p_1\\ \vdots\\ p_{10}\end{bmatrix}-\begin{bmatrix}\delta_1\\ \delta_2\\ \delta_3\end{bmatrix}=0;\ \text{where } \mathbf{N}=\begin{bmatrix}\mathbf{A}_1 & 0 & 0\\ 0 & 1 & -1\end{bmatrix} \tag{24}$$

and the work equation would equate to:

$$\mathbf{g}^{\mathrm{T}}=f_{\mathrm{y}}lt\begin{bmatrix}\mathbf{A}_2 & k & k\end{bmatrix} \tag{25}$$

3.2 | Fasteners

Timmers [26] described a procedure to model bolts in DLO. In his procedure, the bolts were not modelled explicitly but instead the bolt holes were modelled by evenly distributing the ultimate bolt shear $F_{\mathrm{v,Rd}}$ or tension $F_{\mathrm{t,Rd}}$ capacity around the perimeter, determined from [29]. To treat bolt holes, the plate surfaces were divided into a series of convex sub-domains, following the procedure of domain decomposition proposed by He and Gilbert [32]. In the bolt yield criteria, bending was not considered and no interaction between the shear and tension resistance was assumed. In this case the plastic flow matrix for a potential discontinuity of length l can be written as:

$$\mathbf{Np}-\mathbf{d}=\begin{bmatrix}1 & -1 & 0 & 0\\ 0 & 0 & 1 & -1\end{bmatrix}\begin{bmatrix}p_1\\ p_2\\ p_3\\ p_4\end{bmatrix}-\begin{bmatrix}\delta_2\\ \delta_3\end{bmatrix}=0 \tag{26}$$

and the internal work for the energy dissipated by the bolts is written as:

$$\mathbf{g}^{\mathrm{T}}=l\begin{bmatrix}f_{\mathrm{v,b}} & f_{\mathrm{v,b}} & f_{\mathrm{t,b}} & f_{\mathrm{t,b}}\end{bmatrix} \tag{27}$$

This allows for tension in both directions and hence indirectly allows for bearing at the bolt hole. It can be modified to allow for unbounded or zero bearing resistance. In such cases the tension direction is determined from the normal direction of the discontinuity line or sub-domain. The work equation term for the tension force per unit length in the bolt $f_{\mathrm{t,b}}$ is obtained from the tensile resistance of the bolt given by Equation A2, and equates to:

$$f_{\mathrm{t,b}}=\frac{F_{\mathrm{t,Rd}}}{n_{\mathrm{s,b}}l} \tag{28}$$

where $n_{\mathrm{s,b}}$ is an even number of sides of the bolt hole in the DLO model. The equations derived from EN 1993-1-8 [29] are all listed in Appendix A. The work equation terms for the shear force per unit length in the bolt $f_{\mathrm{v,b}}$ are obtained from the shear strength of the bolt given by Equation (A1), and equates to:

$$f_{\mathrm{v,b}}=\frac{F_{\mathrm{v,Rd}}}{\phi_{\mathrm{h}}} \tag{29}$$

where ϕ_h is the bolt hole diameter. However combined shear and tension resistance can still be modelled with caution in DLO, using Equation (A3). When the shear load is vertical downwards the plastic flow matrix in DLO can be written as:

$$\mathbf{Np}-\mathbf{d}=\begin{bmatrix} -1 & -1 & 1 & 1 & 0 & 0 \\ -\dfrac{\alpha_r f_{\mathrm{v,b}}}{1.4 f_{\mathrm{t,b}}} & \dfrac{\alpha_\mathrm{r} f_{\mathrm{v,b}}}{1.4 f_{\mathrm{t,b}}} & -\dfrac{\alpha_\mathrm{r} f_{\mathrm{v,b}}}{1.4 f_{\mathrm{t,b}}} & \dfrac{\alpha_\mathrm{r} f_{\mathrm{v,b}}}{1.4 f_{\mathrm{t,b}}} & 1 & -1 \end{bmatrix}\begin{bmatrix} p_1 \\ p_2 \\ p_3 \\ p_4 \\ p_5 \\ p_6 \end{bmatrix}-\begin{bmatrix} \delta_2 \\ \delta_3 \end{bmatrix}=0 \tag{30}$$

A modification factor is introduced to adjust the shear resistance $f_{\mathrm{v,b}}$ depending on the orientation angle α_r of the discontinuity line with respect to vertical direction of the shear load. The corresponding work matrix for combined shear and tension is obtained from:

$$\mathbf{g}^\mathrm{T}=l\left[\alpha_\mathrm{r} f_{\mathrm{v,b}}\ \ \alpha_\mathrm{r} f_{\mathrm{v,b}}\ \ \alpha_\mathrm{r} f_{\mathrm{v,b}}\ \ \alpha_\mathrm{r} f_{\mathrm{v,b}}\ \ f_{\mathrm{t,b}}\ \ f_{\mathrm{t,b}}\right] \tag{31}$$

where the modification factor α_r is determined from:

$$\alpha_\mathrm{r}=\left(n_{\mathrm{s,b}}\sin\frac{\pi}{n_{\mathrm{s,b}}}\cos\theta_\mathrm{r}\right)^{-1} \text{ where } \theta_\mathrm{r}=\frac{r\pi}{n_{\mathrm{s,b}}} \text{ for } r=1,3\ldots\frac{n_{\mathrm{s,b}}}{2}-1 \tag{32}$$

3.3 | Point and Surface Contact Formulations

Stress resultants at discontinuities can be handled in various ways, as indicated in Figure 8. A surface representation involving the use of a single integration point at the centre of the discontinuity furnishes six unknown displacements and rotations at each such point. The flow rule is formulated for axial and shear deformation interaction, axial deformation and moment rotation interaction, and out-of-plane shear. Twisting moments are in this case not considered. Alternatively, a point representation involves dividing the contact area into e.g., four equal areas, with an integration point coinciding with the centroids of each of these areas. This is referred to as a 4 point contact. A more accurate formulation can be obtained by dividing the thickness of the surface using four rather than two points, giving rise to an 8 point contact. In all multi-point contact formulations there are three displacements at each point. The displacement δ_3 is treated independently. Point formulations have the advantage that twisting moments can now be easily modelled, that were omitted from the surface formulation. The flow matrix can be obtained directly from the yield criteria by transposing this and introducing plastic multipliers to ensure positive energy dissipation. For the point contact formulation a relationship between rotations and displacements is established. In this case the flow rule equation in DLO, $\mathbf{Nd}-\mathbf{p}=0$, is now replaced by the following constraint, where a local $\mathbf{D}$ matrix is derived for each point:

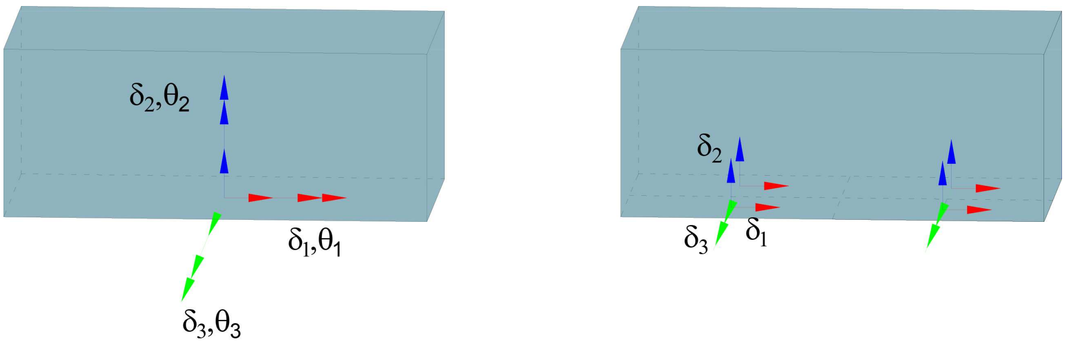

(a) (b)

FIGURE 8 | Discontinuity modelling strategies: (a) surface representation (3 local deformations and 3 local rotations); (b) point representation (3 local deformations at 4 points in this case).

$$\mathbf{Id}_{\boldsymbol{\delta}} + \mathbf{Dd}_{\boldsymbol{\theta}} - \mathbf{Cp} = 0; \quad \mathbf{I}\begin{bmatrix} \delta_1 \\ \delta_2 \\ \delta_3 \end{bmatrix} + \mathbf{D}\begin{bmatrix} \theta_1 \\ \theta_2 \\ \theta_3 \end{bmatrix} - \mathbf{C}\begin{bmatrix} p_1 \\ \vdots \\ p_{10} \end{bmatrix} = 0; \quad \mathbf{C} = \begin{bmatrix} \mathbf{A}_1 & 0 & 0 \\ 0 & -1 & 1 \end{bmatrix}; \quad \mathbf{D} = \begin{bmatrix} 0 & \alpha\frac{t}{4} & 0 \\ \alpha\beta\frac{t}{4} & 0 & -\alpha\frac{l}{4} \\ 0 & -\alpha\frac{l}{4} & 0 \end{bmatrix} \tag{33}$$

where this constraint also incorporates an independent relation for out-of-plane shear/deformation, and where α and β can take a value of 1 or −1, and the local work equation becomes:

$$\mathbf{g}^{\mathrm{T}} = \frac{f_y l t}{4}\begin{bmatrix} \mathbf{A_2} & k & k \end{bmatrix} \tag{34}$$

where $\mathbf{A_1}$ and $\mathbf{A_2}$ are taken from Equations (22) and (23) respectively, and where $k = 1/2$ for the Tresca criterion and $k = 1/\sqrt{3}$ for the Von Mises criterion.

4 | Numerical Examples

The described DLO analysis procedure is now applied to a wide range of examples, including: a plate; rectangular hollow sections (RHS) and circular hollow sections (CHS) subject to axial force and bending moment; a cylindrical shell subject to radial uniform external pressure; a long cylinder subject to ring and band load; a circular plate subject to uniform pressure; a spherical cap under radial uniform load; a plate with holes or notches under tension; a plate with one hole under tension with varying edge distance; an unstiffened T-stub with two or four holes under tension or shear and with varying edge distance or plate thickness; double angle cleats under tension; end plate connections subject to tensile load; an example including combined shear and moment; and finally a metal assembly made of different components. Note that compatible units of mm, N, and MPa are adopted here to ensure well-scaled numerical values, thereby improving the numerical stability of the solver.

In the examples both point and surface contact formulations are used. Different axial moment M-N yield criteria using a square or linearized interaction involving eight linear segments are used for the surface contact formulation. Although the use of more linear segments is possible, eight were chosen in this study as they achieve a favourable balance between computational efficiency, numerical stability, and modelling accuracy. The shear and axial force V-N interaction based on Tresca or Von Mises formulation are used for both point and surface contact formulations. Fasteners are modelled under shear, tension and combined shear and tension.

In general, typical failure mechanisms for in-plane loaded plates are due to combinations of compression, tension and shear forces, leading to net section failure, local buckling, block tearing, bearing resistance of the plate and shear failure of bolts. Typical failure mechanisms for plates loaded out-of-plane are generally due bending failure with plate, web or flange yielding and bolt tension failure. Combined failures also include bolt failure in combined shear and tension. Note that the current DLO formulation precludes the potential for buckling.

This section presents the numerical examples and results, while the findings are discussed in Section 4.9. In all result figures, red and blue discontinuity lines denote positive and negative rotations/deformations, respectively, while green discontinuity lines indicate bolt deformations. Also note that the discontinuity lines are illustrated on the undeformed geometry.

4.1 | Members Subject to Axial Force and Bending Moment

4.1.1 | Plate Subject to Axial Force and Bending Moment

The yield surface for a rectangular plate of breadth b and thickness t in Figure 9a is given in Appendix C. A verification has been carried out using DLO, for a simply supported rectangular plate having a yield stress $f_y = 275$ MPa, breadth $b = 100$ mm, thickness $t = 50$ mm and length $l = 1000$ mm, subject to five particular load cases of permanent axial load applied over the ends and variable uniformly distributed load over the whole length. The distributed load was applied both in-plane and out-of-plane. Results are presented in Table 1 and plotted in Figure 10.

4.1.2 | Hollow Section Subject to Axial Force and Bending Moment

The yield surface for a thin rectangular hollow section with centreline dimensions of breadth b, depth d and thickness t and of a thin circular hollow section of radius r in Figure 9 are given in Appendix D and Appendix E respectively. A

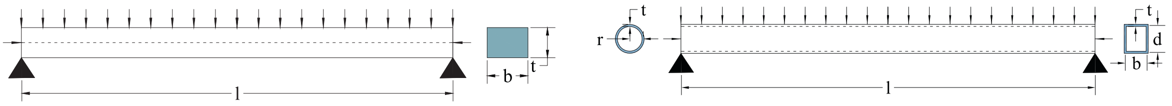

(a) (b)

FIGURE 9 | (a) Plate and (b) RHS/CHS subject to axial force and bending moment.

TABLE 1 | Members subject to axial force and bending moment: deviation of moment from yield surface for various DLO formulations.

			DLO							
			Surface contact				**Point contact**			
	Equations		**Square M-N Int.**		**Linearized M-N Int.**		**4 point**		**8 point**	
Case	***n******	***m******	***m******		***m******		***m******		***m******	
Plate	0.00	1.0000	1.0000	0.00%	1.0000	0.00%	1.0000	0.00%	1.0000	0.00%
(out-of-plane)	0.25	0.9375	1.0000	6.67%	0.8409	−10.30%	0.7500	−20.00%	0.8750	−6.67%
Equation (C1)	0.50	0.7500	1.0000	33.33%	0.7500	0.00%	0.5000	−33.33%	0.7500	0.00%
	0.75	0.4375	1.0000	128.57%	0.3750	−14.29%	0.2500	−42.85%	0.3750	−14.29%
	1.00	0.0000	0.0000	0.00%	0.0000	0.00%	0.0000	0.00%	0.0000	0.00%
Plate (in-plane)	0.00	1.0000	1.0000	0.00%	1.0000	0.00%	1.0000	0.00%	1.0000	0.00%
Equation (C1)	0.25	0.9375	1.0833	15.56%	0.9375	0.00%	0.9305	−0.74%	0.9305	−0.74%
	0.50	0.7500	0.8889	18.52%	0.7500	0.00%	0.7500	0.00%	0.7500	0.00%
	0.75	0.4375	0.5833	33.34%	0.4375	0.00%	0.4305	−1.59%	0.4305	−1.59%
	1.00	0.0000	0.0000	0.00%	0.0000	0.00%	0.0000	0.00%	0.0000	0.00%
RHS	0.00	1.0000	1.0526	5.26%	0.9868	−1.32%	0.9868	−1.32%	0.9868	−1.32%
Equation (D1)	0.25	0.9178	0.9671	5.38%	0.9045	−1.44%	0.9045	−1.44%	0.9045	−1.44%
	0.50	0.6798	0.7237	6.45%	0.6653	−2.13%	0.6610	−2.77%	0.6646	−2.24%
	0.75	0.3673	0.3947	7.46%	0.3617	−1.53%	0.3620	−1.46%	0.3620	−1.46%
	1.00	0.0000	0.0000	0.00%	0.0000	0.00%	0.0000	0.00%	0.0000	0.00%
CHS	0.00	1.0000	1.1407	14.07%	0.9970	−0.30%	0.9970	−0.30%	0.9970	−0.30%
Equation (E1)	0.25	0.9239	1.0650	15.27%	0.9248	0.10%	0.9211	−0.31%	0.9216	−0.24%
	0.50	0.7071	0.8499	20.20%	0.7137	0.93%	0.7086	0.21%	0.7086	0.21%
	0.75	0.3827	0.5281	37.99%	0.4001	4.56%	0.3921	2.47%	0.3921	2.47%
	1.00	0.0000	0.0000	0.00%	0.0000	0.00%	0.0000	0.00%	0.0000	0.00%

verification has been carried out using DLO for a simply supported RHS and CHS having a yield stress $f_y = 275$ MPa, breadth $b = 100$ mm, depth $d = 100$ mm, radius $r = 50$ mm, wall thickness $t = 20$ mm, length $l = 1000$ mm, subject to five load cases involving a fixed axial load applied to the ends and variable uniformly distributed load over the whole length. Results are presented in Table 1 and plotted in Figure 11.

4.2 | Cylindrical Shells

4.2.1 | Cylindrical Shell Subject to Radial Uniform External Pressure

The yield surface for a cylindrical shell, simply supported and built-in at both ends subject to radial uniform positive external pressure p, with radius r, thickness t, length l and yield stress f_y in Figure 12, is given in Appendix F has been studied by Paul and Hodge [33]. The results for a cylinder with centreline dimensions of $r = 1.0$ m, and thickness $t = 0.020$ m, length $l = 4$ m and yield stress $f_y = 275$ MPa are presented in Table 2 and Figure 13.

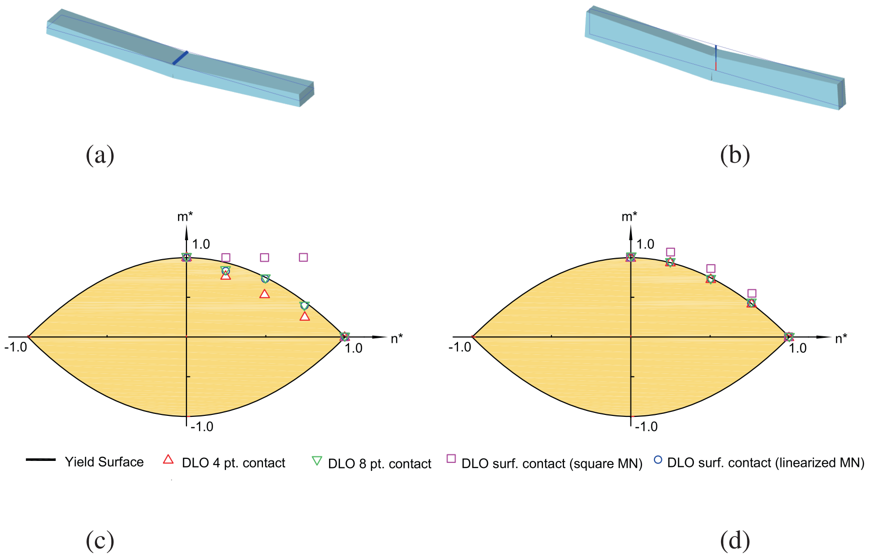

FIGURE 10 | Plate subject to axial force and bending moment: (a) deformed shape under out-of-plane bending; (b) deformed shape under in-plane bending; (c) M-N values for various cases under out-of-plane bending; (d) M-N values for various cases under in-plane bending. (Discontinuity lines are shown on the undeformed geometry).

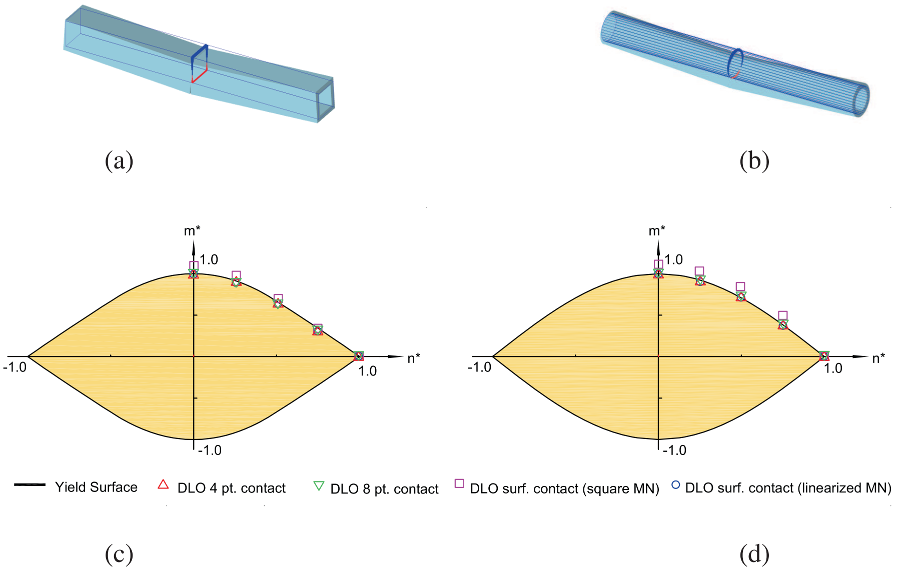

FIGURE 11 | RHS & CHS subject to axial force and bending: (a) deformed shape of RHS; (b) deformed shape of CHS; (c) M-N values for various cases for RHS; (d) M-N values for various cases for RHS.

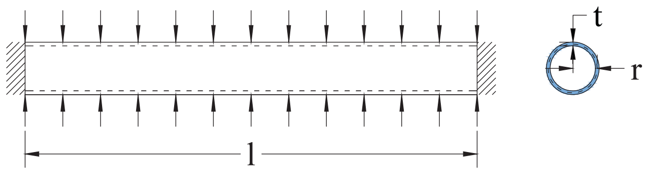

FIGURE 12 | Cylindrical shell subject to radial uniform external pressure: Details.

TABLE 2 | Cylindrical shell subject to radial uniform external pressure: comparison of pressures p (MPa) between DLO (100 nodes and 300 potential discontinuities) and equations for simple and fixed edge conditions.

	pressures p (MPa)						
		DLO					
		Surface					
Support	**Equations**	**Square M-N Int.**		**Linearized M-N Int.**		**Point**	
Simple	5.507 (F1)	8.255	49.898%	5.222	−5.166%	5.508	0.015%
Fixed	5.514 (F1)	8.268	49.961%	5.521	0.139%	5.521	0.139%

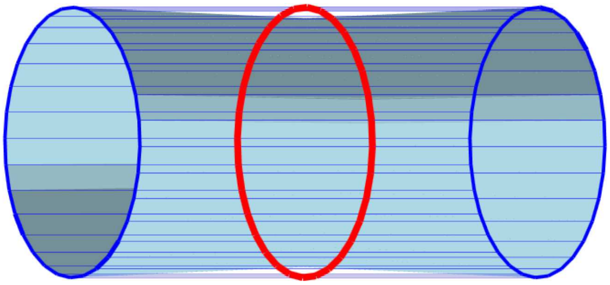

FIGURE 13 | Cylindrical shell subject to radial uniform external pressure: Failure mechanism.

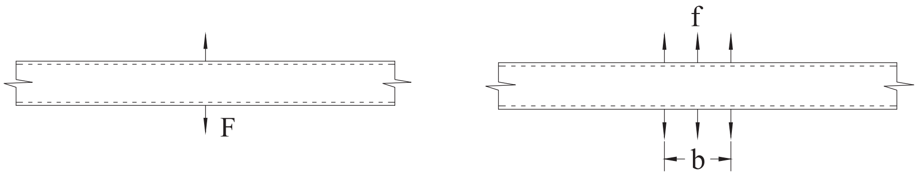

(a)

(b)

FIGURE 14 | Cylindrical shell subject to: (a) ring load; (b) band load.

TABLE 3 | Cylindrical shell subject to ring or band load: Comparison of failure loads F and distance between hinges L between equations and DLO (circa 1000 nodes and 6000 potential discontinuity lines).

	Equations		**DLO**		
Load	**L (m)**	**F (kN/m)**	**L (m)**	**F (kN/m)**[a]	**F (kN/m)**[b]
Line	0.224 (G4)	1118.0 (G5)	0.220	1202.351	1124.312
Band	0.381 (G8)	1905.0 (G9)	0.375	2021.760	1904.701

[a] Square M-N interaction.

[b] Linearized M-N interaction.

4.2.2 | Cylindrical Shell Subject to Ring or Band Load

The yield surface for a long metal cylinder that is ring-loaded or band-loaded has been studied by Calladine [34]. The yield surfaces for a cylinder with radius r, thickness t, and yield stress f_y under a ring-load of F, or a uniform band load f over a band width b as in Figure 14, where $F = bf$ per unit circumferential length, are given in Appendix G. The results for a cylinder with centreline dimensions of $r = 2.0$ m, and thickness $t = 0.025$ m, band width $b = 0.5$ m and yield stress $f_y = 200$ MPa are presented in Table 3 and Figure 15.

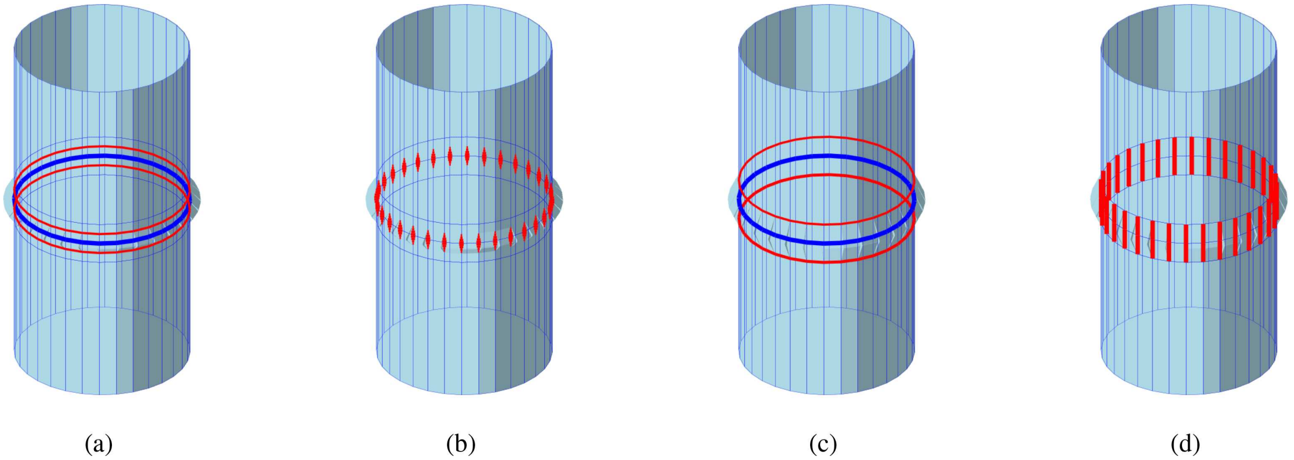

(a) (b) (c) (d)

FIGURE 15 | Cylindrical shell subject to ring or band load: (a) rotational failure mechanism for ring load case; (b) circumferential failure mechanism for ring load case; (c) rotational failure mechanism for band load case; (d) circumferential failure mechanism for band load case.

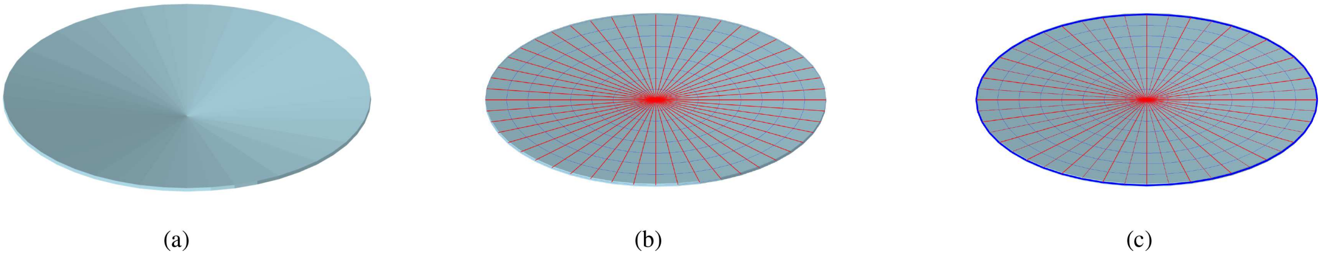

(a) (b) (c)

FIGURE 16 | Circular plate subject to uniform pressure: (a) deformed plate at failure; (b) rotational failure mechanism with simple supports; (c) rotational failure mechanism with fixed supports.

4.3 | Circular Plate and Spherical Cap

4.3.1 | Circular Plate Subject to Uniform Pressure

The failure load of a circular plate subjected to a uniformly distributed load p, having radius r, and thickness t, hinged or fixed at the edge has been cited in Save and Massonnet [21] is given in Appendix H. The results using DLO for a circular plate with varying radii r, thickness $t = 20$ mm, yield stress $f_y = 250$ MPa and are presented in Figure 16. A comparison between the results using Equation (I1) and DLO is presented in Figure 17. The results for a circular plate for simple and fixed supports using a square and linearized M-N interaction, point contact are very similar and are very close to the results provided in the literature, indicating that the three methods produce similar results when there is no combination of bending moment or axial force.

4.3.2 | Spherical Cap Under Radial Uniformly Distributed Load

The failure load of a spherical cap subjected to radial uniformly distributed load p, having radius r and thickness t, and subtending a cap angle of 2α, hinged or fixed at the edge has been obtained by Hodge [35], and cited in Save and Massonnet [21], is represented in Figure 18 and given in Appendix I. The results using DLO for a spherical cap with varying cap angle are presented for a thick walled cap having radius $r = 1000$ mm, thickness $t = 20$ mm, yield stress $f_y = 250$ MPa and are presented in Figure 19. A comparison between the results using Equations (I1) and (I2) and DLO is presented in Figure 20. The results for a spherical cap for simple and fixed supports using a square M-N interaction are very close to the results provided in the literature. When using the linearized M-N interaction or the point contact formulation the normal surface pressure is slightly smaller for small cap angles.

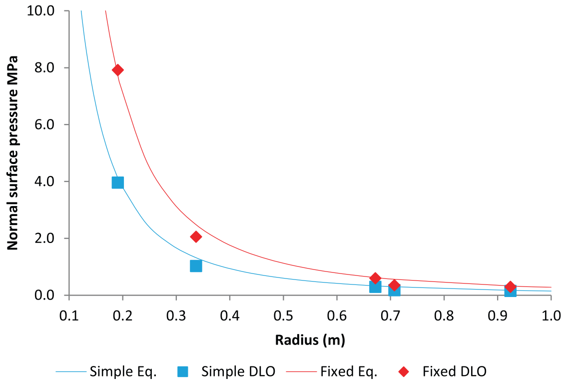

radius (m)	p (MPa)			
	Equations		DLO Surface/Point	
	(H34) Simple	(H34) Fixed	Simple	Fixed
0.195	3.941	7.403	3.958	7.916
0.383	1.024	1.924	1.029	2.057
0.707	0.300	0.564	0.301	0.603
0.924	0.176	0.330	0.177	0.353
1.000	0.150	0.282	0.151	0.301

FIGURE 17 | Circular plate subject to uniform pressure: Comparison of pressures p (MPa) with radius (m), for DLO (400 nodes and 1500 potential discontinuities) for surface (square or linearized M-N interaction) and point contact formulations, and Equation (H1), for simple and fixed supports.

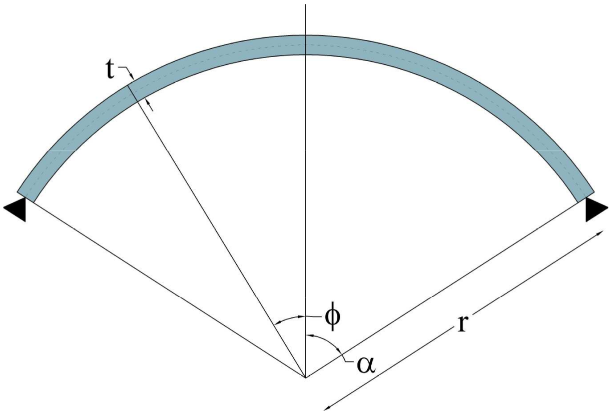

FIGURE 18 | Spherical cap under radial uniformly distributed load.

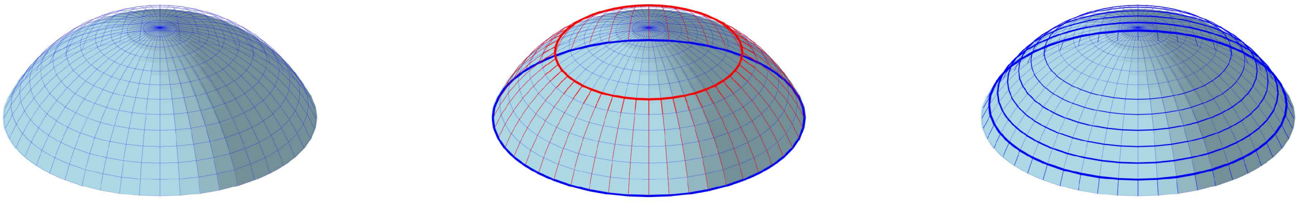
(a)
(b)
(c)

FIGURE 19 | Metal spherical cap ($3\pi/8$) (a) deformed cap at failure (b) rotational failure (c) deformational failure mechanism.

4.4 | Rectangular Plate

4.4.1 | Plate Under Tension With/Without Holes or Notches

The in-plane failure of a plate under tension with two notches or with one hole was studied using the Von Mises yield criterion and the Tresca yield criterion. The plate has a yield stress $f_y = 355$ MPa, length $l = 250$ mm, breadth $b = 100$ mm, thickness $t = 8$ mm and diameter of notch or hole of 40 mm. The results are presented in Figure 21 and Table 4. The plate examples without or with holes and notches and the following examples of unstiffened T-stub were extensively studied by Timmers [26, 27] using 2D DLO. The tensile failure load using DLO based on the linearized V-N interaction in Figure 7b are very close to the values obtained by FEA and quoted in Timmers [26] using a displacement driven non-linear analysis and solid elements and a bilinear material behaviour. The values obtained by Timmers [26] using DLO were based on the

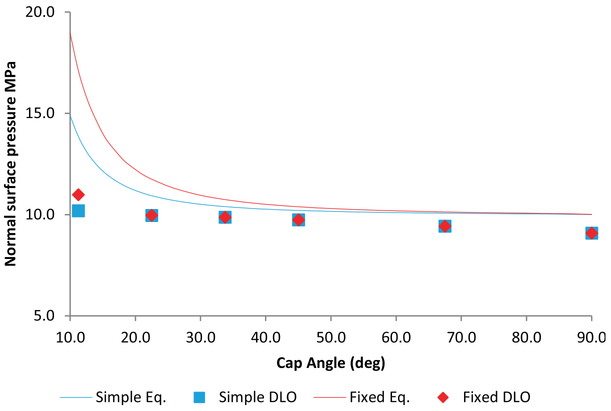

Cap Angle α ($\pi/16$)	p (MPa)			
	DLO			Equations (I35)† (I36)‡
	Surface		Point	
	Square MN	Linearized MN		
Simple†				
1	14.342	10.422	10.189	13.851
2	11.121	9.994	9.960	10.933
3	10.710	9.927	9.866	10.392
4	10.497	9.847	9.743	10.203
6	10.288	9.648	9.435	10.067
8	10.120	9.416	9.082	10.001
Fixed‡				
1	18.212	13.382	10.977	17.108
2	12.206	10.061	9.962	11.747
3	11.109	9.928	9.866	10.742
4	10.710	9.847	9.743	10.386
6	10.372	9.648	9.435	10.130
8	10.150	9.418	9.082	10.013

FIGURE 20 | Metal spherical cap: Comparison of pressures p (MPa) with cap angle (deg) between DLO (circa 600 nodes and 3000 potential discontinuities) using a square M-N interaction, a linearized M-N interaction, point formulation and Equations (I1) & (I2) for simple and fixed bearings.

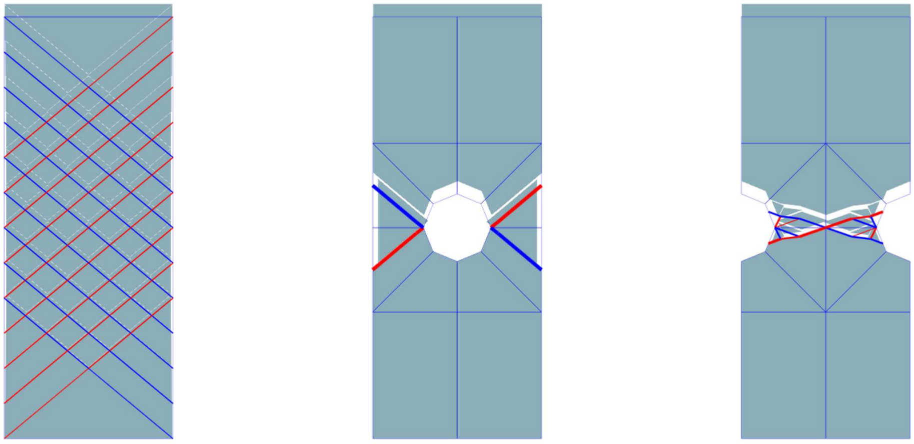
(a) (b) (c)

FIGURE 21 | Deformational failure mechanism using Tresca or Von Mises yield criterion for tensile specimen (a) plain, (b) with hole (c) with notch.

TABLE 4 | Tensile failure load (kN) for plate, plate with hole, notched plate, under Tresca or Von Mises linearized V-N yield criterion with equations and DLO (circa 500 nodes, 9000 potential discontinuity lines) using either surface or point formulation.

	Tensile failure load F_t (kN)								
	Tresca				**Von Mises**				
Case	**DLO**	**FEA**[b]	$F_{t,1}$[a]	$F_{t,2}$[a]	**DLO**	**FEA**[b]	$F_{t,1}$[a]	$F_{t,2}$[a]	**Equations**
Plain	283.366	284.7	284.000	284.000	317.510	284.2	284.000	327.935	(J1)
Hole	170.328	169.8	170.400	170.400	190.736	170.5	170.400	196.761	(J2)
Notched	200.391	171.8	170.400	219.994	207.491	191.7	170.400	254.027	(J3)

[a] Appendix J [26].
[b] FEA result by [26].

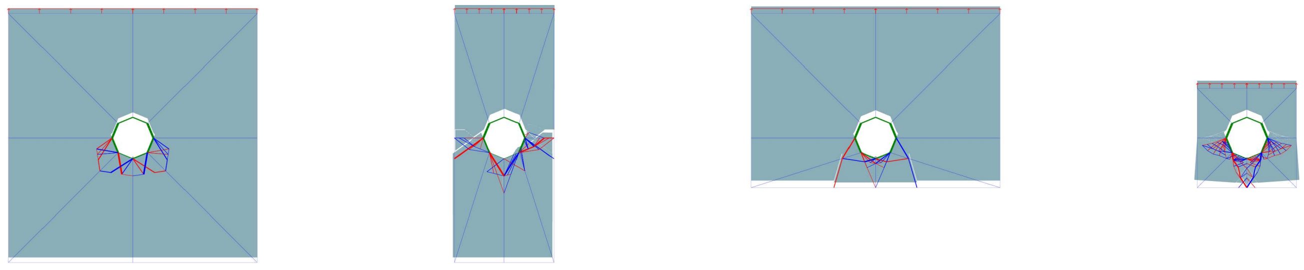
(a) (b) (c) (d)

FIGURE 22 | Deformational failure mechanism using Tresca or Von Mises yield criterion for plate with one hole under tension with varying edge distances; Table 5.

TABLE 5 | Comparison of failure load (kN) for a plate with one hole under tension with varying edge distances using DLO (400 nodes and 6000 potential discontinuities) for surface or point interaction and equations.

			***F* (kN)**				
	Edge Dist. (mm)		**DLO**		**FEA[a]**	**Equations**	
Case	e_1	e_2	**Tresca**	**Von Mises**	**Von Mises**	$F_{\mathrm{b,Rd}}(A4)$	$V_{\mathrm{eff,1,Rd}}(A6)$
(a)	66.0	66.0	84.219	88.717	86.100	**156.800**	310.464
(b)	66.0	26.4	67.459	74.080	77.300	104.115	**86.930**
(c)	26.4	66.0	63.809	70.283	69.300	**62.720**	310.464
(d)	26.4	26.4	56.044	62.753	62.700	**41.646**	86.930

[a] [26].

simple V-N interaction in Figure 7a and are the same as those reported in the equations for $F_{t,1}$ or pure tension failure in Appendix J.

4.4.2 | Plate With One Hole Under Tension With Varying Edge Distances

The in-plane failure of a plate with a yield stress $f_y = 355$ MPa, with one grade 8.8, 20 mm diameter bolt in 22 mm diameter hole was studied for four edge distances in 8 mm plate thickness, as presented by Timmers [26]. The different failure modes using DLO, in plate bearing, bolt shear, plate shear, and plate tearing and shear are shown in Figure 22. The results obtained from DLO are presented in Table 5 where e_1 and e_2 are the vertical and horizontal edge distance from the centre of the hole. The results were compared to Equation (A4) for bolt bearing and Equation (A6) for block tearing resistance. Timmers [26] reported a failure load of 63.3 kN using Tresca or Von Mises criterion using the simple V-N interaction and proposed applying a higher yield strength for zones in compression to increase the bearing strength. The is evidently not required when using the linearized V-N interaction as the results obtained are very close to the results obtained by FEA and reported in Timmers [26]. Failure by tearing resistance is only evident for smaller values of edge distances.

4.5 | Unstiffened T-Stub

4.5.1 | Unstiffened T-Stub With Two Holes Under Tension With Varying Plate Thickness

The out-of-plane failure of a T-stub under tension with varying thickness, bolted to a fixed stiff base was studied. The T-stub flange plate had a flange plate of length $l_p = 200$ mm and breadth $b_p = 80$ mm with two 18 mm holes and two 16 mm grade 8.8 bolts, and a web plate with thickness t_w =10 mm. The edge distance $e = n = 50$ mm and $m = 40$ mm where n and m are defined in section 6.2.4 of EN 1993-1-8 [29]. Figure 23 shows three different modes of failure that include; failure mode 1, by complete flange yielding; failure mode 2, with tensile bolt failure and flange yielding; failure mode 3, with bolt tensile failure. The DLO model has 1275 nodes and 36,724 potential discontinuity lines and uses either a surface (square or linearized M-N interaction) or point formulation. In the study of T-stub connections, a

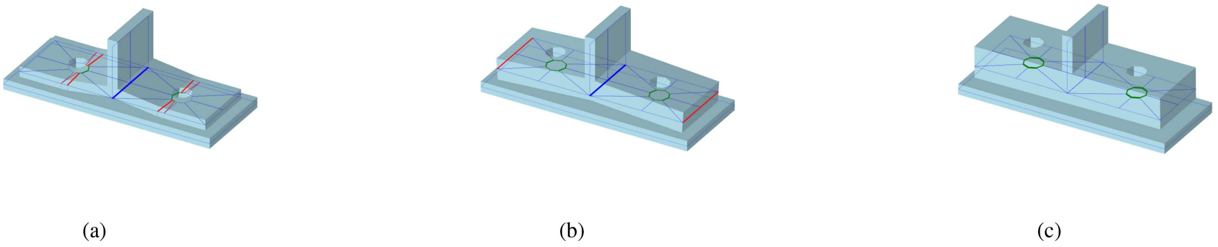
(a) (b) (c)

FIGURE 23 | Rotational failure mechanism: Flange bending or tension bolt yielding failure; (a) Mode 1 flange yielding $t_p = 10$ mm $F_{T,1,Rd} = 44.86$ kN (DLO), (b) Mode 2 bolt failure with flange yielding $t_p = 20$ mm $F_{T,2,Rd} = 127.67$ kN (DLO), (c) Mode 3: Bolt tensile failure $t_p = 30$ mm $F_{T,3,Rd} = 180.75$ kN (DLO).

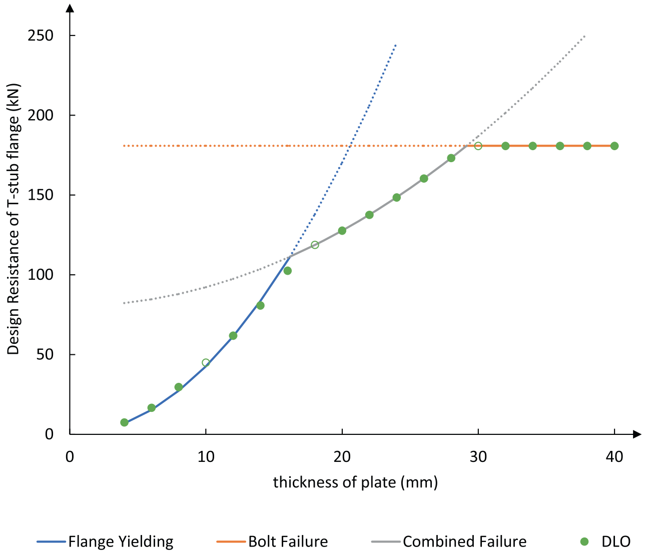

FIGURE 24 | Comparison of ultimate load of T-stub vs plate thickness results using equations; flange yielding Equation (A9), bolt failure with flange yielding Equation (A10), bolt failure Equation (A11) and DLO.

compression only contact in bearing has been implemented to model contact between the bearing plates so as to allow for lift off.

The results are compared with the design resistance of a T-stub flange using EN 1993-1-8 [29] for the primary three modes of failure. The resistance for complete flange yielding $F_{T,1,Rd}$ is obtained from Equation (A9), the resistance for bolt failure with flange yielding $F_{T,2,Rd}$ is obtained from Equation (A10), and the resistance for bolt failure $F_{T,3,Rd}$ is obtained from Equation (A11). The results are presented in Figure 24.

4.5.2 | Unstiffened T-Stub With Two Holes Under Shear and Tension

A stiff T-stub as shown in Figure 25a under combined shear and tension forces was tested so as to compare the combined forces at failure using DLO with Equation (A3) in EN 1993-1-8 [29] for combined failure of bolts under tension and shear. The dimensions of T-stub were chosen such as to have failure solely in the bolts and to prevent failure by bending of the plate. The plate has a length $l_p = 160$ mm, breadth $b_p = 80$ mm and thickness $t_p = 20$ mm, with two 22 mm diameter holes and two 20 mm grade 4.6 bolts. The DLO model has 1275 nodes and 36,724 potential discontinuity lines and uses either a surface (square or linearized M-N interaction) or point formulation. The results between DLO and Equation (A3) are plotted in Figure 25b. The results obtained in DLO closely match the values obtained using the shear tension interaction equation.

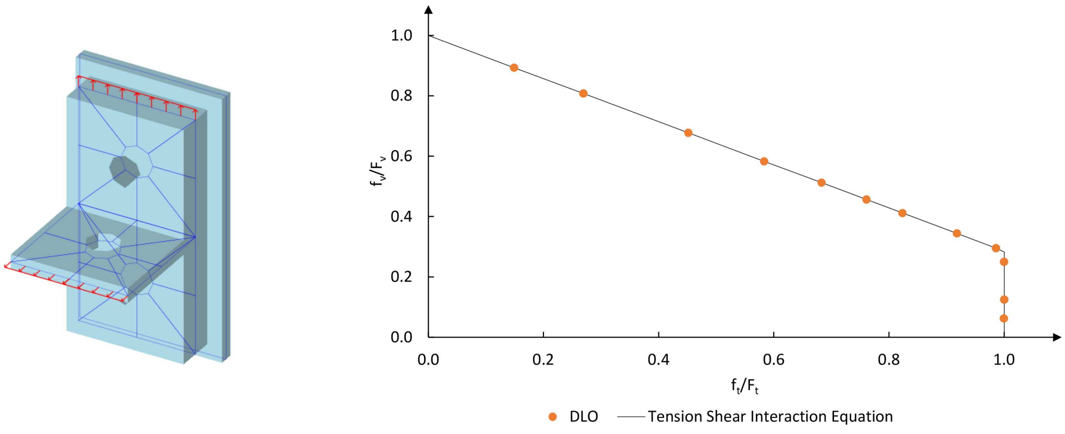

(a) (b)

FIGURE 25 | (a) T-stub specimen under tension and shear loading (b) Comparison of shear tension interaction (Equation A3) with results obtained from DLO.

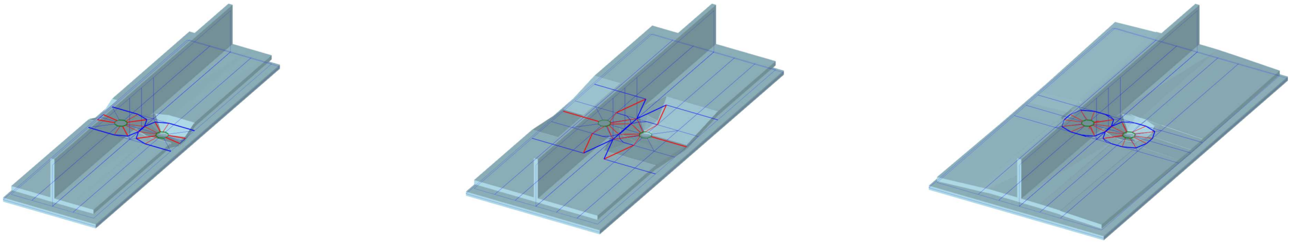

(a) (b) (c)

FIGURE 26 | Rotational failure mechanism and deformed geometry (a) T-stub 600 mm × 160 mm, (b) T-stub 600 mm × 240 mm, (c) T-stub 600 mm × 320 mm.

4.5.3 | Unstiffened T-Stub With Two Holes Under Tension With Varying Edge Distance

The out-of-plane failure of a T-stub under tension with varying breadth of plate b_p and edge distance e, bolted to a fixed stiff base was studied. The T-stub has a length of plate l_p = 600 mm, web thickness t_w = 10 mm, flange thickness t_p = 10 mm, plate yield stress f_y = 275 N/mm^2, two 22 mm holes with two 20 mm grade 8.8 bolts, m = 40 mm and n varies between 40 mm, 80 mm and 120 mm. The plate and bolt dimensions were chosen so as to study mode 1 failure, complete flange yielding without any bolt failure or prying, for circular and non-circular local failure patterns. The results obtained from the DLO models were compared with results obtained using EN 1993-1-8 [29] of a T-stub flange $F_{T,1,Rd}$ using Equation (A9). The effective lengths are determined from Table 6.4 of EN 1993-1-8 [29] 'Effective lengths for an unstiffened column', where l_{eff} is equivalent to the minimum of $4m + 1.25e$, $2\pi m$, $\pi m + 2e_1$ for Mode 1. The different failure modes are shown in Figure 26 and the results are shown in Figure 27.

4.5.4 | Unstiffened T-Stub With Four Holes Under Tension

A T-stub with 4 holes under tension with varying length of plate l_p has also been studied. The T-stub has a flange plate with breadth b_p = 160 mm, web thickness t_w = 8 mm, flange thickness t_p = 8 mm, plate yield stress f_y = 275 N/mm^2, four 22 mm holes with four 20 mm grade 8.8 bolts. Double curvature complete flange yielding is the predominant failure modes as shown in Figure 28. As the length of the T-stub increases, the yield line is no longer parallel to the web but fans around the end bolts to the sides. The different failure modes are shown in Figure 28 and the results are shown in Figure 29.

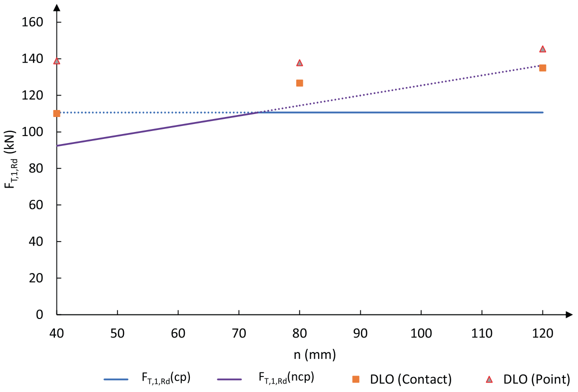

Case	edge dist. e (mm)	breadth b_p (mm)	DLO F(kN) Surface	Point	$F_{T,1,Rd}$(kN) Eq. (A9)
(a)	40	160	110.088	138.898	92.400 †
(b)	80	240	126.682	137.827	110.584 ‡
(c)	120	320	135.000	145.440	110.584‡

‡ non-circular pattern, † circular pattern

FIGURE 27 | Comparison of the ultimate loads of a simple T-stub using Equation (A9) for non-circular and circular local failure patterns under tension with varying edge distance with DLO for surface contact (600 nodes, 6000 discontinuities) and point contact formulation (200 nodes, 1000 discontinuities).

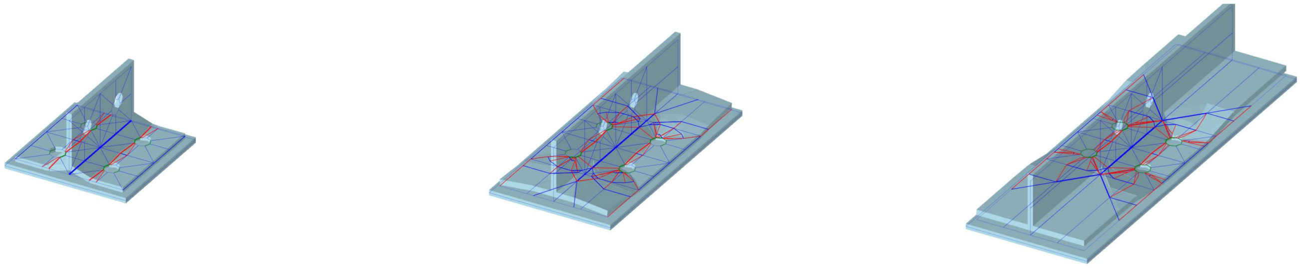

(a) (b) (c)

FIGURE 28 | Rotational failure mechanism and deformed (a) T-stub 160 mm × 160 mm, (b) T-stub 320 mm × 160 mm, (c) T-stub 520 mm × 160 mm.

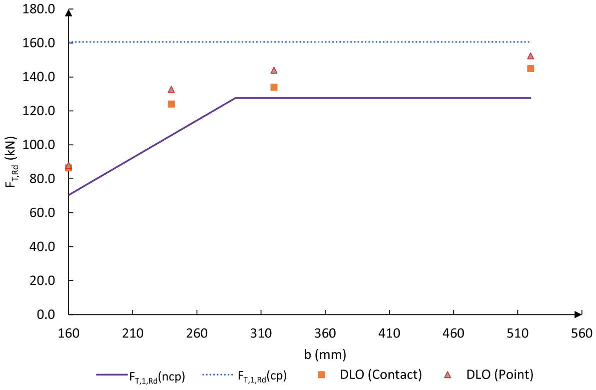

Case	b(mm)	DLO F(kN) Surface	Point	Eq. (A9) $F_{T,1,Rd}(kN)$
(a)	160	86.417	87.904	70.400
(b)	240	124.075	132.721	105.600
	320	133.883	143.980	127.600
(c)	520	144.887	152.442	127.600

FIGURE 29 | Ultimate tensile load (kN) for T-stub with four holes and varying width using Equations A9 and DLO for surface contact (1000 nodes and 12000 discontinuities) and point contact formulation (300 nodes and 1200 discontinuities).

4.6 | Double Angle Cleats Under Tension

Double angle cleats with 2 holes under tension with varying breadth b have also been studied. The double equal angles are 80 mm × 80 mm, thickness $t = 6$ mm, with a yield stress $f_y = 355$ N/mm^2, and have two 22 mm holes with two 20 mm grade 10.9 bolts. Single curvature complete flange yielding is the predominant failure modes as shown in Figure 30. As the length of the angle section increases the yield line is no longer parallel to the web but fans around the end bolts to the sides. The different failure modes are shown in Figure 30 and the results are shown in Figure 31.

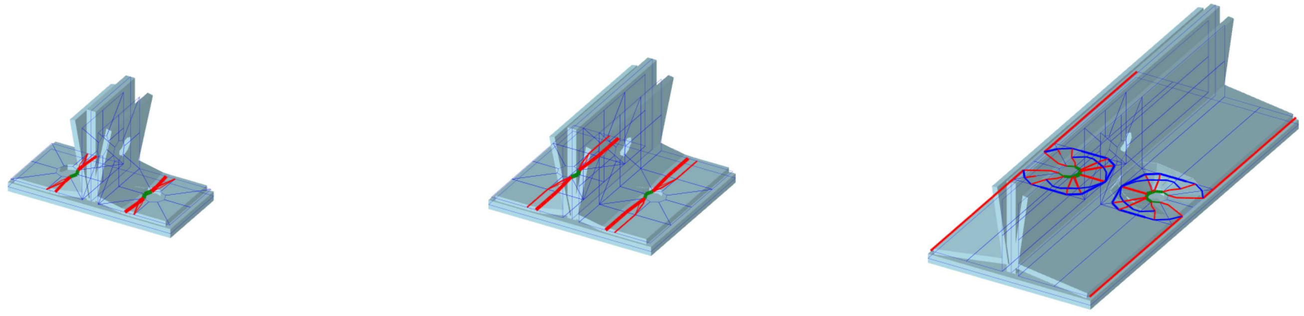
(a) (b) (c)

FIGURE 30 | Rotational failure mechanism and deformed geometry for double angle cleats with dimensions (a) b = 80 mm, (b) b = 160 mm, (c) b = 400 mm.

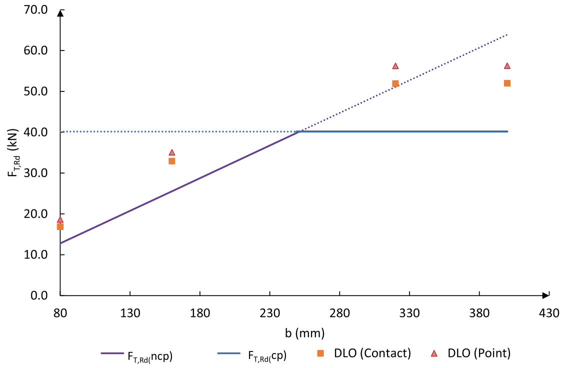

Case	b(mm)	DLO F(kN) Surface	Point	Eq. (A9) $F_{\mathrm{T,1,Rd}}(kN)$
(a)	80	16.877	18.653	12.780
(b)	160	32.960	35.089	25.560
	320	51.912	56.261	51.120
(c)	400	52.029	56.263	63.900

FIGURE 31 | Ultimate tensile load (kN) for twin angle cleats with 2 holes with varying width using Equation (A9) and DLO.

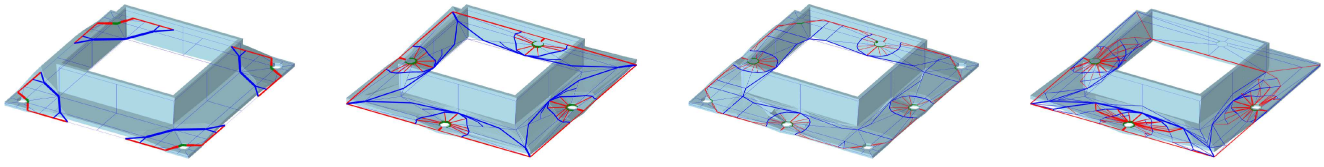
(a) (b) (c) (d)

FIGURE 32 | Rotational failure mechanism and deformed geometry for end plate to SHS (a) in tension with 4 bolts at the corners (b) in tension with 4 bolts at the sides (c) in tension with 8 bolts (d) in bending with 4 bolts at the sides.

4.7 | End-Plate Connections Subject to Axial Load, Shear and Moment

Timmers [36] used 2D DLO to extensively study end-plate connections to RHS members in tension, and concluded that EN 1993-1-8 [29] does not provide any design rules for such connections. A SHS end-plate connection and a CHS end-plate connection have both been studied here, under tension only and under combined action of shear and moment. A SHS 200 × 6 mm with an end-plate having dimensions 320 × 320 × 6 mm with 18 mm diameter holes and grade 8.8 16 mm diameter bolts along with a CHS 200 × 6 with an end-plate having a radius of 160 mm and thickness of 6 mm, with 18 mm diameter holes and grade 8.8 16 mm diameter bolts have been modelled. For tension only a uniform pressure was applied on the perimeter of the section, and for bending a uniform horizontal line pressure was applied along the perimeter of the section, 50 mm above the connection interface. The different failure modes for the SHS and CHS are shown in Figures 32 and 33 respectively, and the results are shown in Table 6. A clear advantage of the shell DLO formulation is that combined failure in-plane and out-of-plane can be easily handled. In this case rotation in the section walls can also be modelled.

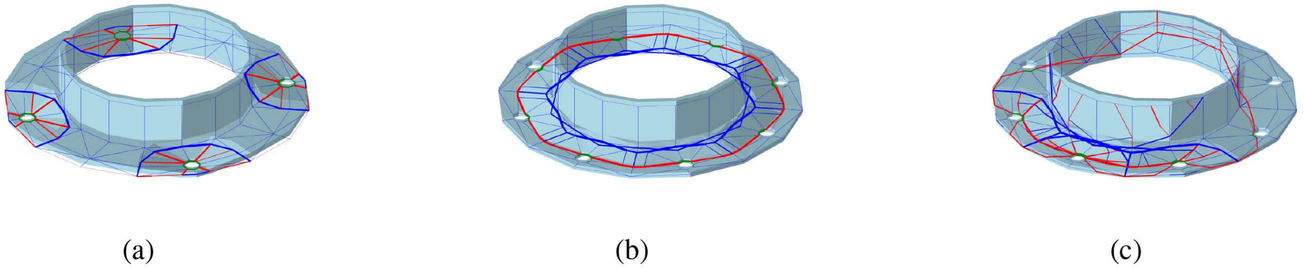

FIGURE 33 | Rotational failure mechanism and deformed geometry for end plate to CHS (a) in tension with 4 bolts (b) in tension with 8 bolts (c) in bending with 8 bolts.

TABLE 6 | Ultimate tensile load (kN) for T-stub with four holes and varying width using Equation (A9) and DLO.

Case	Figure	F (kN)	No. Nodes	No. Discs	Time (mins)[a]
SHS	(a)	61.536	1024	11200	0.47
	(b)	140.088	736	8000	0.37
	(c)	159.149	1344	14400	71.27
	(d)	15.554	803	8211	48.88
CHS	(a)	170.196	1488	16064	86.30
	(b)	103.111	1184	11904	78.78
	(c)	15.275	1492	16070	23.07

[a] AMD Ryzen 7 5700U 1.80 GHz processor.

4.8 | Metal Assembly

A metal assembly connecting a beam to a column using a T-stub bolted connection is studied. Steel connections are assembled from different components that consist of plates, welds and bolts. The connections are generally loaded in-plane or out-of-plane or a combination of both. EN 1993-1-8 [29] specifies design rules for single components.

The component has been modelled with the following geometrical and material properties. Bolt size $\phi_b = 20$ mm, bolt hole $\phi_h = 22$ mm, bolt grade 10.9, thickness of flange plate $t_f = 15$ mm, thickness of fin plate $t_f = 15$ mm and the plate yield stress $f_y = 275$ N/mm^2, were utilized unless otherwise stated. The dimensions of the plates in the assembly are shown in Figure K1.

The shell DLO model considers the beam, the T-stub and the column as independent components that are related to one another by enforcing conditions. Special attention needs to be taken when more than two domains meet at a boundary to ensure compatibility. A bearing only at the bottom of the stub flange is enforced with the column and no bolts are used in the lower row of the flange plate. The action load in the beam is applied as two equal and equivalent loads on the bolt holes of the fin plate of the stub and on the top notched part of the web of the beam as in Figure 34a. In this way the failure in the weaker component can be determined automatically from the analysis. The following in-plane and out-of-plane failure modes can be induced on the assembly:

- Bolt shear: in-plane failure. To model in-plane shear of the web bolts, a grade 4.6 bolt was used in the fin plate connection. The failure mode using DLO is represented in Figure 34b and the results in Table 7. The ultimate load for this failure is $2F_{v,Rd}$.
- Block shear or tearing: in-plane failure. The failure mode using DLO for block shear or tearing failure in the fin plate is represented in Figure 34c and the results in Table 7. The ultimate load for this failure is $V_{eff,1,Rd}$.
- Bearing resistance: in-plane failure. A bearing failure in the fin plate is picked up with a denser mesh and when the bearing resistance of the bolt is smaller than the shear resistance of a bolt. A grade 10.9 bolt was used in the fin

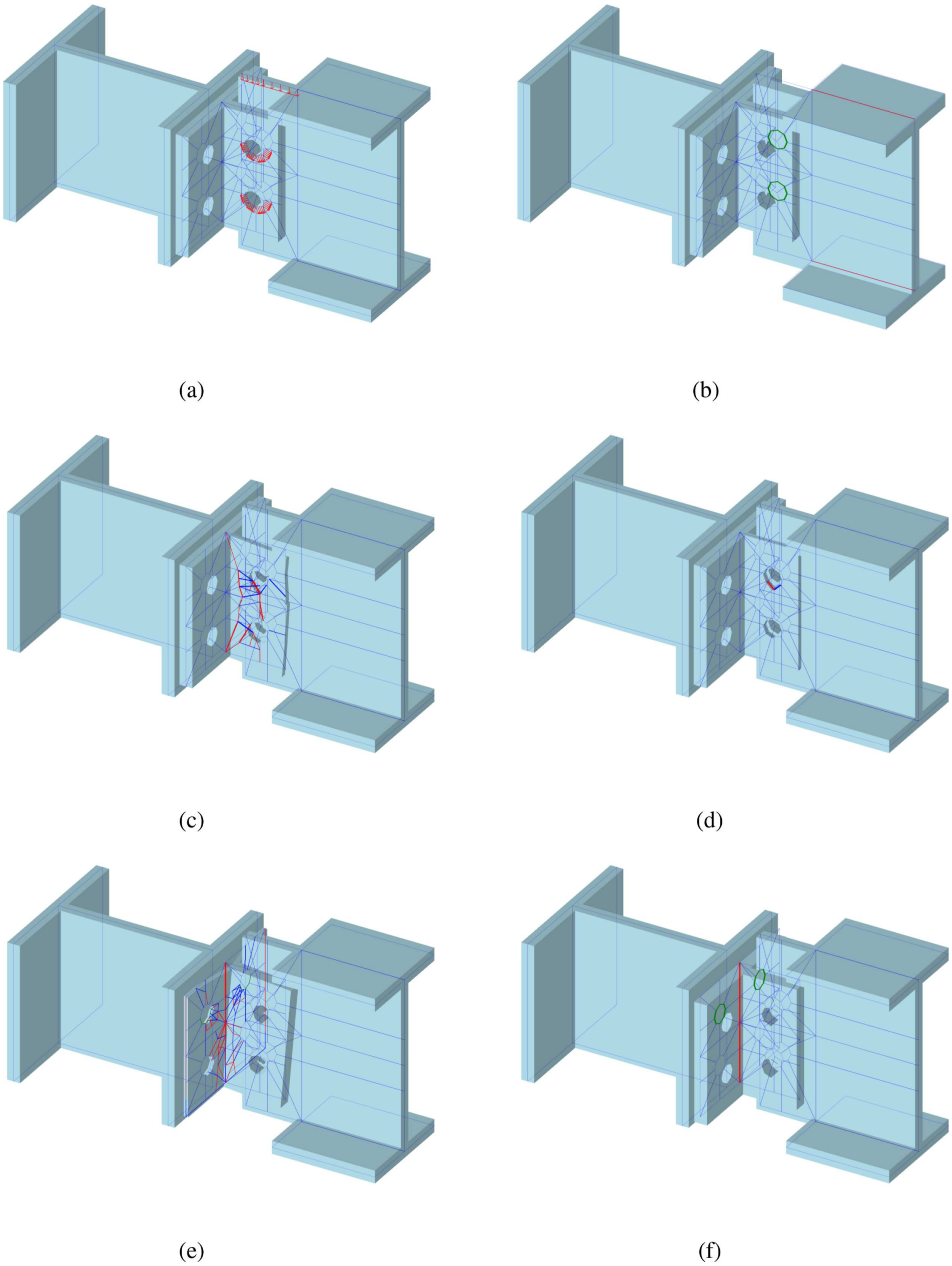

FIGURE 34 | Failure modes of assembly using DLO: (a) equivalent loads on assembly; (b) bolt shear failure (in-plane); (c) block shear tearing plate failure (in-plane); (d) bolt bearing failure; (e) stub plate bending failure (out-of-plane); (f) combined tension and shear bolt failure (out-of-plane).

TABLE 7 | Comparison of failure loads for different failure modes of the assembly with DLO.

Case	Failure mode	DLO F (kN)	Equation F (kN)	Difference
Figure 34b	Bolt shear	94.063	94.080	−0.018%
Figure 34c	Block shear or tearing	296.956	262.368	13.183%
Figure 34d	Bearing resistance	307.697	309.600	−0.615%
Figure 34e	Plate bending	89.164	96.113	−7.230%
Figure 34f	Combined tension and shear	89.262	77.495	15.185%

plate. The failure mode using DLO is represented in Figure 34d and the results in Table 7. The ultimate load can be determined from $2F_{\mathrm{b,Rd}}$.

- Plate bending: out-of-plane failure. Mode 1, complete flange yielding of the flange plate is reproduced by reducing the flange thickness t_{f} to 5 mm. The failure mode using DLO is represented in Figure 34e and the results in Table 7. The respective lever arm of the loads in the horizontal and vertical direction are $h = 40$ mm and $v = 89$ mm. The ultimate load can be determined from equilibrium using $F_{\mathrm{T,1,Rd}}v/h$.
- Combined tension and shear: out-of-plane failure. Combined tension shear failure of the flange bolts is obtained by using a thicker fin plate of 15 mm. The respective lever arm of the loads in the horizontal and vertical direction are $h = 40$ mm and $v = 89$ mm. The ultimate load can be determined from equilibrium using $2F_{\mathrm{v,Rd}}/(1 + F_{\mathrm{v,Rd}}h/1.4F_{\mathrm{t,Rd}}v)$.

4.9 | Commentary

Solutions derived from theoretical equations were compared with those obtained using DLO employing both point contact and surface contact formulations, together with various idealizations of the applicable yield criteria. The results demonstrate that the most suitable idealization is problem dependent. For example, Table 8 summarizes the M–N interaction idealizations that were found to be most appropriate for the examples considered.

For problems exhibiting limited interaction between axial force and bending moment, the surface contact formulation with a square moment–axial force interaction idealization provides accurate results with relatively short computational times. However, when significant axial force–moment interaction is present, this formulation becomes inaccurate and nonconservative, as shown in Figure 10a,c. Despite this limitation, it remains computationally efficient, as it requires the smallest number of constraints and variables in the DLO formulation.

As expected, the use of a linearized M–N interaction idealization yields more accurate results. For problems involving combined out-of-plane bending and axial force interaction, accuracy can be further improved by increasing the number of segments used to linearize the yield surface. In contrast, for problems dominated by in-plane bending, accuracy is more sensitive to the discretization of the section, with improvements achieved by increasing the number of nodal divisions. This effect is clearly illustrated in Figure 10b,d where seven nodes were used across the plate depth.

The point contact formulation generally produces reasonably accurate results, albeit at the expense of increased computational cost due to the larger number of optimization variables. Its accuracy decreases for problems involving significant axial force–moment interaction under out-of-plane loading, as shown in Figure 10a,c. Nevertheless, accuracy can be improved by subdividing the section into thinner strips, as demonstrated by the eight point contact results presented in Figure 10a,c.

TABLE 8 | Suitability of moment vs axial force (M-N) interaction idealizations for the example problems considered.

Surface contact formulation—square M-N interaction	Surface contact formulation—linearized M-N interaction/point contact formulation
Cylindrical shell subject to ring or band load 4.2.2	Plate, RHS, CHS subject to axial force and bending moment 4.1
Circular plate subject to uniform pressure 4.3.1	Cylindrical shell subject to radial uniform external pressure 4.2.1
Plate without or with holes or notches under tension and with varying edge distances 4.4	Spherical cap under radial uniformly distributed load 4.3.2
Unstiffened T-stub 4.5	
Double angle cleats under tension 4.6	
End plate connections subject to axial load, shear and moment 4.7	
Metal assembly 4.8	

In summary, both formulations are valid and effective but require a linearization of at least eight linear segments when there is an M-N interaction. For the V-N interaction eight linear segments were always used and both the point contact and surface contact formulations gave similar results. An advantage of the point contact formulation is that twisting moments are more straightforward to model, and only a single, comprehensive yield surface is required, rather than multiple uncoupled yield surfaces as in the surface contact formulation. The point contact formulation is generally easier to implement and more flexible, particularly for complex loading conditions, but incurs a modest increase in computational cost compared to the surface contact approach.

For an assembly, the failure load is currently generally obtained by determining the lowest load factor after exploring a number of failure yield patterns tabulated in EN 1993-1-8 [29] and determining the resistance of each individual component. The method is laborious as the local resistance of single components have to be obtained before arriving at the global resistance of the steel assembly. The DLO thin-walled analysis approach can be successfully used to directly identify the lowest load factor and critical failure mechanism for an assembly loaded both in-plane and out-of-plane. The results presented here have been validated against results obtained from EN 1993-1-8 [29], showing that these collapse loads and failure mechanisms can be reproduced correctly. Also, for end plate connections connected to a CHS or RHS in tension, shear and bending, EN 1993-1-8 [29] does not give any guidance.

It has been demonstrated that the results using linearized V-N interaction idealization with Tresca or Von Mises yield criteria produce more accurate results than those produced by Timmers [26], which were based solely on the uniaxial relationship between the shear stress and yield stress, or used a simple square V-N interaction. The results eliminate the need to modify the yield strength to take account of bearing resistance, reported by Timmers. Both the Tresca and Von Mises criteria give similar results, with the Tresca model being slightly more conservative.

The shell DLO formulation has the advantage that connections including components such as angle web cleats, end plates and fin plate connections can be modelled. Special attention needs to be taken when more than two domains meet at a boundary to ensure compatibility. Using 2D DLO, the stiffness of the web member is considered as infinite by assuming no bending along the line of the web member, and this is imposed on the model by using deformation constraints. With the shell DLO formulation this assumption is not required and hence a more realistic simulation can be performed. At the intersection of the T-stub, a rigid sub-domain may be introduced to better model the additional stiffness at the intersection, which would be more consistent with the definition of the internal distance m defined in EN 1993-1-8 [29]. The rigid subdomain was not incorporated in the results but can be introduced within the physical overlapping thickness of the sub-domain by preventing or ignoring any failure along the discontinuity lines.

The DLO procedure has the advantage that it can automatically identity upper bound failure mechanisms, obviating the need for these to assume predefined failure planes. The number of mechanisms captured depends on the accuracy and number of flow criteria. More accurate results can be obtained by refining the nodal grid and number of discontinuities. The results produced were obtained using a moderate number of nodal divisions and number of potential discontinuities and the time to obtain a solution was generally between a second and a few minutes. The computational performance can be enhanced by using adaptive techniques, such as the ‘member adding’ and geometry optimization procedures that have been applied previously [32]. An adaptive procedure similar to that proposed by Smith and Gilbert [19] can also potentially be implemented to improve the model of the yield criteria at each iteration.

The present study has focused on thin-walled shells. Thick-walled shells are more complex to analyse. DLO has already been applied to solid three-dimensional plasticity problems by Hawksbee et al. [15], where unlike a discontinuity line formulation, a surface discontinuity formulation in the form of polygons was used. This enhancement would be interesting to employ when one needs to focus on the failure of a particular zone in a shell. The DLO formulation can also employ curved elements and curved discontinuity lines rather than planar elements and straight discontinuity lines. This would obviate the need to use a smeared thickness at the intersection of the planar sub-domains. The formulation may also be extended to account for buckling effects. For instance, a second-order FEM with geometric imperfections could first be performed to determine the corresponding stress state, which is then employed within the DLO framework. Alternatively, buckling may be incorporated by modifying the DLO failure envelope using the elastic critical buckling stress obtained from a FE buckling analysis. Such extensions, however, would substantially increase the methodological complexity and computational cost, and are therefore left for future research.

This study recognises several limitations. Curved surfaces are represented using multiple planar facets, such that curved discontinuity lines are approximated by piecewise-linear segments. In addition, the full coupling among bending moments, axial forces, and shear forces is approximated through two separate interactions, namely M–N and V–N coupling. Finally, it is assumed that σ_y in Equation (B1) is zero along any discontinuity. Consequently, when failure is governed by regional rather than line-type mechanisms under the Von Mises yield criterion, this assumption may lead to either conservative or non-conservative estimates of the material strength.

5 | Conclusions

Discontinuity layout optimization (DLO) is a numerical limit analysis procedure that has previously been applied to in-plane, out-of-plane and 3D problems. In this work a new shell formulation is presented to allow problems simultaneously involving in-plane and out-of-plane failure to be modelled. The new formulation is applied to a range of example problems involving metal components and assemblies formed from thin plates or shells. It is demonstrated that the DLO procedure can produce good estimates of the failure load when an appropriate numerical discretization and idealization of the applicable yield criteria is adopted.

The study suggests that the DLO procedure can provide a viable alternative to more complex analysis tools, such as non-linear finite element analysis, when the failure load of a component or assembly formed from thin plates or shells is sought. With finite elements materially non-linear problems require the use of an incremental solution procedure which can be prone to numerical problems; also singularities in the stress or displacement field can be challenging to model, typically requiring remeshing. In contrast, with DLO the failure load can be computed directly, without iterative solutions, and since the method is formulated entirely in terms of discontinuities it can produce accurate solutions for problems involving singularities.

Acknowledgments

Professor Matthew Gilbert passed away before the submission of this manuscript. He contributed significantly to the development of the work, and his coauthorship is included with deep respect and gratitude.

Data Availability Statement

The data that support the findings of this study are available from the corresponding author upon reasonable request.

References

1. J. Chakrabarty, *Applied Plasticity. Mechanical Engineering Series* (Springer US, 2010).

2. J. Chakrabarty, *Theory of Plasticity* (Elsevier, 2012).

3. G. J. Vegte, J. Wardenier, and R. S. Puthli, “FE Analysis for Welded Hollow-Section Joints and Bolted Joints,” *Proceedings of the Institution of Civil Engineers* 163, no. 6 (2010): 427–437.

4. X. Zhao, “Yield Line Mechanism Analysis of Steel Members and Connections,” *Progress in Structural Engineering and Materials* 5, no. 4 (2003): 252–262.

5. B. K. J. Hiriyur and B. W. Schafer, “Yield-Line Analysis of Cold-Formed Steel Members,” *International Journal of Steel Structures* 5, no. 1 (2005): 43–54.

6. H. S. Y. Chan, “The Collapse Load of Reinforced Concrete Plate,” *International Journal for Numerical Methods in Engineering* 5, no. 1 (1972): 57–64.

7. J. Munro and A. M. A. Da Fonseca, “Yield Line Method by Finite Elements and Linear Programming,” *Structural Engineer* 56B, no. 2 (1978): 37–44.

8. K. V. Balasubramanyam and V. Kalyanaraman, “Yield-Line Analysis by Linear Programming,” *Journal of Structural Engineering* 114, no. 6 (1988): 1431–1437.

9. D. Johnson, “Yield-Line Analysis by Sequential Linear Programming,” *International Journal of Solids and Structures* 32, no. 10 (1995): 1395–1404.

10. W. A. M. Alwis, “Discrete Element Slip Model of Plasticity,” *Engineering Structures* 22, no. 11 (2000): 1494–1504.

11. W. S. Dorn, “Automatic Design of Optimal Structures,” *Journal de mécanique* 3 (1964): 25–52.

12. C. C. Smith and M. Gilbert, “Application of Discontinuity Layout Optimization to Plane Plasticity Problems,” *Proceedings of the Royal Society of London. Series A: Mathematical and Physical Sciences* 463 (2007): 2461–2484.

13. M. Gilbert, L. He, C. C. Smith, and C. V. Le, "Automatic Yield-Line Analysis of Slabs Using Discontinuity Layout Optimization," *Proceedings of the Royal Society A: Mathematical, Physical and Engineering Sciences* 470, no. 2168 (2014): 20140071.

14. Z. Sun, Y. Zhang, Y. Yuan, and H. A. Mang, "Stability Analysis of a Fire-Loaded Shallow Tunnel by Means of a Thermo-Hydro-Chemo-Mechanical Model and Discontinuity Layout Optimization," *International Journal for Numerical and Analytical Methods in Geomechanics* 43, no. 16 (2019): 2551–2564.

15. S. Hawksbee, C. Smith, and M. Gilbert, "Application of Discontinuity Layout Optimization to Three-Dimensional Plasticity Problems," *Proceedings of the Royal Society. A, Mathematical, Physical and Engineering Sciences* 469, no. 2155 (2013): 20130009.

16. Y. Zhang, "Multi-Slicing Strategy for the Three-Dimensional Discontinuity Layout Optimization (3D DLO)," *International Journal for Numerical and Analytical Methods in Geomechanics* 41, no. 4 (2017): 488–507.

17. M. Gilbert and A. Tyas, "Layout Optimization of Large-Scale Pin-Jointed Frames," *Engineering Computations* 20, no. 8 (2003): 1044–1064.

18. L. He, "Rationalization of Trusses and Yield-Line Patterns Identified Using Layout Optimization," (PhD Thesis, University of Sheffield, 2015).

19. C. C. Smith and M. Gilbert, "Identification of Rotational Failure Mechanisms in Cohesive Media Using Discontinuity Layout Optimization," *Géotechnique* 63, no. 14 (2013): 1194–1208.

20. Y. Zhang, X. Wang, X. Wang, and H. A. Mang, "Virtual Displacement Based Discontinuity Layout Optimization," *International Journal for Numerical Methods in Engineering* 123, no. 22 (2022): 5682–5694.

21. M. A. Save and C. E. Massonnet, *Plastic Analysis and Design of Plates, Shells and Disks* (North Holland Publishing Company, 1972).

22. M. P. Nielsen and L. C. Hoang, *Limit Analysis and Concrete Plasticity* (CRC Press, 2019).

23. A. Shalloway and J. R. Trott, *Design Patterns Explained: A New Perspective on Object-Oriented Design*, 2nd ed. (Pearson Education India, 2005).

24. M. De Berg, O. Cheong, M. Van Kreveld, and M. Overmars, "Computational Geometry: Introduction," in *Computational Geometry: Algorithms and Applications* (Springer, 2008), 1–17.

25. C. Hua, "An Inverse Transformation for Quadrilateral Isoparametric Elements: Analysis and Application," *Finite Elements in Analysis and Design* 7, no. 2 (1990): 159–166.

26. R. Timmers, "Application of Discontinuity Layout Optimization to Steel Parts and Steel Connections With a Single Bolt," *Applied Sciences* 10, no. 11 (2020): 3783.

27. R. Timmers, "Generalized Method for Identifying Yield-Line Patterns in T-Stubs Using Discontinuity Layout Optimization," *Engineering Structures* 244 (2021): 112802.

28. L. He, M. Gilbert, and M. Shepherd, "Automatic Yield-Line Analysis of Practical Slab Configurations via Discontinuity Layout Optimization," *Journal of Structural Engineering* 143, no. 7 (2017): 04017036.

29. BS EN 1993-1-8 2005, *Eurocode 3: Design of Steel Structures - Part 1–8: Design of Joints* (British Standards Institute, 2005).

30. M. B. Wong, *Plastic Analysis and Design of Steel Structures* (Butterworth-Heinemann, 2011).

31. W. Johnson and P. B. Mellor, *Engineering Plasticity* (John Wiley & Sons, 1983).

32. L. He and M. Gilbert, "Automatic Rationalization of Yield-Line Patterns Identified Using Discontinuity Layout Optimization," *International Journal of Solids and Structures* 84 (2016): 27–39.

33. B. Paul and P. G. Hodge, *Carrying Capacity of Elastic-Plastic Shells Under Hydrostatic Pressure* (Polytechnic Institute of Brooklyn, Department of Aeronautical Engineering, 1957).

34. C. R. Calladine, *Theory of Shell Structures* (Cambridge University Press, 1989).

35. P. G. Hodge, *Limit Analysis of Rotationally Symmetric Plates and Shells* (Prentice-Hall, 1963).

36. R. Timmers and R. Lang, "Yield-Line Mechanisms and Design Proposal for Endplate Connections in Rectangular Hollow Section Members in Tension," *Engineering Structures* 279 (2023): 115560.

37. BS EN 1991–1-1 2005, *Eurocode 3: Design of Steel Structures - Part 1–1: General Rules and Rules for Buildings* (British Standards Institute, 2005).

38. W. F. Chen and T. Atsuta, *Theory of Beam-Columns: In-Plane Behavior and Design* (J. Ross Publishing, 2007).

39. T. V. Galambos, *Guide to Stability Design Criteria for Metal Structures* (John Wiley & Sons, 1998).

40. J. M. Rotter and A. J. Sadowski, "Full Plastic Resistance of Tubes Under Bending and Axial Force: Exact Treatment and Approximations," *Structure* 10 (2017): 30–38.

Appendix A

Equations in EN 1993-1-8:2005 for Bolts, Welds and T-Stubs

Bolts

The shear, bearing, tensile and combined shear and tension resistance of bolts are obtained from Table 3.4 EN 1993-1-8 [29].

The shear resistance of a bolt $F_{\mathrm{v,Rd}}$ is obtained from:

$$F_{\mathrm{v,Rd}} = \frac{0.6 f_{\mathrm{yb}} A_s}{\gamma_{\mathrm{M2}}} \tag{A1}$$

The tension resistance of a bolt $F_{\mathrm{t,Rd}}$ is obtained from:

$$F_{\mathrm{t,Rd}} = \frac{0.9 f_{\mathrm{ub}} A_s}{\gamma_{\mathrm{M2}}} \tag{A2}$$

The combined shear and tension resistance of a bolt must satisfy:

$$\frac{F_{\mathrm{v,Ed}}}{F_{\mathrm{v,Rd}}} + \frac{F_{\mathrm{t,Ed}}}{1.4 F_{\mathrm{t,Rd}}} \leq 1 \tag{A3}$$

The bearing resistance of a bolt $F_{\mathrm{b,Rd}}$ is obtained from (general equation):

$$F_{\mathrm{b,Rd}} = \frac{k_1 \alpha_{\mathrm{b}} f_{\mathrm{u}} d t}{\gamma_{\mathrm{M2}}} \tag{A4}$$

where α_{b} is the smallest of α_d, $f_{\mathrm{ub}}/f_{\mathrm{u}}$ or 1.0 where:

$$\alpha_d = \frac{e_1}{3d_0} \text{ for end bolts;} \quad \alpha_d = \frac{p_1}{3d_0} - \frac{1}{4} \text{ for inner bolts}$$

where k_1 is the smallest of $2.8e_2/d_0$-1.7 or 2.5 for edge bolts and the smallest of $1.4p_2/d_0$-1.7 or 2.5 for inner bolts, e_1 is edge distance and p_1 is the pitch in direction of load transfer, e_2 is edge distance and p_2 is the pitch perpendicular to the direction of load transfer.

A simpler equation for bearing resistance $F_{\mathrm{b,Rd}}$ from 3.6.1. 'Bolts and rivets' EN 1993-1-8 [29]:

$$F_{\mathrm{b,Rd}} = \frac{1.5 f_{\mathrm{u}} d t}{\gamma_{\mathrm{M2}}} \tag{A5}$$

The block tearing resistance $V_{\mathrm{eff,Rd}}$ is given in section 3.10.2 of EN 1993-1-8 [29]:

$$V_{\mathrm{eff,1,Rd}} = \frac{f_{\mathrm{u}} A_{\mathrm{nt}}}{\gamma_{\mathrm{M2}}} + \frac{f_{\mathrm{y}}}{\sqrt{3}} \frac{A_{\mathrm{nv}}}{\gamma_{\mathrm{M0}}} \tag{A6}$$

for concentric loading:

$$V_{\mathrm{eff,2,Rd}} = \frac{0.5 f_{\mathrm{u}} A_{\mathrm{nt}}}{\gamma_{\mathrm{M2}}} + \frac{f_{\mathrm{y}}}{\sqrt{3}} \frac{A_{\mathrm{nv}}}{\gamma_{\mathrm{M0}}} \tag{A7}$$

for eccentric loading, where A_{nt} is the net area subject to tension and A_{nv} is the net area subject to shear.

Welds

The design shear strength of a fillet weld $F_{\mathrm{w,Rd}}$ is given in 4.5.3.3 'Simplified method for design resistance of fillet weld', EN 1993-1-8 [29]:

$$F_{\mathrm{w,Rd}} = \frac{f_{\mathrm{u}}}{\sqrt{3} \beta_{\mathrm{w}} \gamma_{\mathrm{M2}}} \tag{A8}$$

where f_{u} is the ultimate tensile strength of the weaker part joined and β_{w} is the appropriate correlation factor taken from Table 4.1. of EN 1993-1-8 [29].

Design Resistance of a T-Stub Flange

The design resistance of a T-stub flange, $F_{\mathrm{t,Rd}}$ may be obtained from Table 6.2 EN 1993-1-8 [29] where three modes of failure where prying forces may develop. The three modes are identified as:

Mode 1—Complete yielding of the flange:

$$F_{\mathrm{T,1,Rd}} = \frac{4M_{\mathrm{pl,1,Rd}}}{m} \tag{A9}$$

Mode 2—Bolt failure with yielding of the flange:

$$F_{\mathrm{T,2,Rd}} = \frac{2M_{\mathrm{pl,2,Rd}} + 2nF_{\mathrm{t,Rd}}}{m+n} \tag{A10}$$

Mode 3—Bolt failure:

$$F_{\mathrm{T,3,Rd}} = 2F_{\mathrm{t,Rd}} \tag{A11}$$

where:

$$M_{\mathrm{pl,1,Rd}} = \frac{l_{\mathrm{eff,1}} t_{\mathrm{f}}^2 f_{\mathrm{y}}}{4\gamma_{\mathrm{M0}}}, \quad M_{\mathrm{pl,2,Rd}} = \frac{l_{\mathrm{eff,2}} t_{\mathrm{f}}^2 f_{\mathrm{y}}}{4\gamma_{\mathrm{M0}}} \tag{A12}$$

and $n = \mathrm{e}_{\min}$ but $n \leq 1.25$ m.

For an end bolt row, from Table 6.4 of EN 1993-1-8 [29] 'Effective lengths for an unstiffened column', l_{eff} is equivalent to the minimum of $4\mathrm{m} + 1.25\mathrm{e}$, $2\pi\mathrm{m}$, $\pi\mathrm{m} + 2\mathrm{e}_1$ for Mode 1 and $4\mathrm{m} + 1.25\mathrm{e}$ for Mode 2.

The following notation has been used: From Table 3.1 EN 1993-1-1 [37], f_{y} is the nominal yield strength of the structural steel and f_{u} is the nominal ultimate strength of the structural steel. From Section 6.1 EN 1993-1-1 [37], γ_{M0}, γ_{M1}, γ_{M2} are the partial safety factor of members and cross-sections. From Table 2.1 EN 1993-1-8 [29], γ_{M2} is the partial safety factor of bolts,welds, plates in bearing. t is thickness of the structural steel, $A_{v,\mathrm{eff}}$ is the effective shear area, $F_{\mathrm{v,Rd}}$ is the design shear resistance per bolt, $F_{\mathrm{t,Rd}}$ is the design tensile resistance per bolt, $F_{\mathrm{v,Ed}}$ is the design shear force per bolt, $F_{\mathrm{t,Ed}}$ is the design tensile force per bolt, d is the nominal bolt diameter, d_0 is the bolt hole diameter, f_{yb} nominal values of bolt yield strength and f_{ub} nominal values of bolt ultimate strength.

Appendix B

Tresca and Von Mises Yield Criterion

The principal stresses at a point on a thin plate can be written as:

$$\sigma_{1,2} = \frac{\sigma_{\mathrm{x}} + \sigma_{\mathrm{y}}}{2} \pm \sqrt{\frac{(\sigma_{\mathrm{x}} - \sigma_{\mathrm{y}})^2}{4} + \tau_{\mathrm{xy}}^2} \tag{B1}$$

Consider a thin plate under axial stress σ and torsional stress τ only. Equation (B1) can be written as:

$$\sigma_{1,2} = \frac{\sigma}{2} \pm \sqrt{\frac{\sigma^2}{4} + \tau^2} \tag{B2}$$

noting that $\sigma = \sigma_{\mathrm{x}}$, $\sigma_{\mathrm{y}} = 0$ and $\tau = \tau_{\mathrm{xy}}$.

Tresca yield criteria is given by:

$$\frac{|\sigma_1 - \sigma_2|}{2} = f_{\mathrm{y}} \tag{B3}$$

Substituting Equation (B2) in the above we can write:

$$\left(\frac{\sigma}{f_{\mathrm{y}}}\right)^2 + \left(\frac{\tau}{f_{\mathrm{y}}/2}\right)^2 = 1 \tag{B4}$$

Von Mises yield criteria is given by:

$$\frac{1}{2}\left\{(\sigma_1 - \sigma_2)^2 + (\sigma_2 - \sigma_3)^2 + (\sigma_3 - \sigma_1)^2\right\} = f_{\mathrm{y}} \tag{B5}$$

Substituting Equation (B2) in the above we can write:

$$\left(\frac{\sigma}{f_{\mathrm{y}}}\right)^2 + \left(\frac{\tau}{f_{\mathrm{y}}/\sqrt{3}}\right)^2 = 1 \tag{B6}$$

Appendix C

Plate Subject to Axial Force and Bending Moment

The yield surface for a rectangular plate of breadth b and thickness t is given by:

$$|m^*| + n^{*2} - 1 = 0 \tag{C1}$$

where m^* and n^* are the dimensionless moments and axial force in Equations (11) and (12), respectively.

Appendix D

Thin RHS Subject to Axial Force and Bending Moment

The yield surface for a thin rectangular hollow section with centreline dimensions of breadth b, depth d and thickness t is given in [38, 39] as:

$$m^* = \begin{cases} 1 - \dfrac{(b+d)^2 n^{*2}}{t^2 + 2bd + d^2} & \text{if } n^* \leq \dfrac{d-t}{b+d} \\ \dfrac{2(b+d)(1-n^*)(t^2 + bd + n^* t(b+d))}{(b+t)(d^2 + 2bd + t^2)} & \text{otherwise} \end{cases} \tag{D1}$$

where:

$$F_{2,\mathrm{Rd}} = 2 f_{\mathrm{y}} (b+d) t, \quad M_{1,\mathrm{Rd}} = \frac{f_{\mathrm{y}} t (d^2 + 2bd + t^2)}{2} \tag{D2}$$

Appendix E

Thin CHS Subject to Axial Force and Bending Moment

The yield surface for a thin circular hollow section with centreline dimensions of radius r and thickness t is given in [40] as:

$$n^* = \frac{2cos^{-1} m^*}{\pi} \tag{E1}$$

where:

$$F_{2,\mathrm{Rd}} = 2\pi r t f_{\mathrm{y}}, \quad M_{1,\mathrm{Rd}} = 4 r^2 t f_{\mathrm{y}} \tag{E2}$$

Appendix F

Cylindrical Shell

The failure load of a cylindrical shell subject to radial uniformly distributed load p, having radius r and thickness t, subject to radial uniform positive external pressure, has been derived by Paul and Hodge [33] and is given when the element is simply supported at both ends ($k = 1$), and built in at both ends ($k = 2$) as:

$$p = \frac{f_{\mathrm{y}} t}{r} \left(1 + \frac{1}{1 + \dfrac{l^2}{ktr}} \right) \tag{F1}$$

Appendix G

Ring-Loaded and Band-Loaded Long Cylinder

The yield surface for a metal ring-loaded or band-loaded long cylinder has been studied by [34] with radius r, thickness t and yield stress f_{y}. The yield criterion can be determined using kinematics, by equating the energy dissipated at the yield lines with the work done by the load. At yield three parallel circumferential hinges form that are spaced apart by a distance l. The rotations at the outer yield line is δ / l and at the inner yield line $2\delta / l$ where δ is a lateral displacement. The mean rate of energy dissipation over the length by stretching is $\delta l / r$. Using the work equations for a ring-loaded cylinder with a ring load F per unit circumferential length:

$$F\delta = 4 M_{1,\mathrm{Rd}} \frac{\delta}{l} + F_{2,\mathrm{Rd}} l \frac{\delta}{r} \tag{G1}$$

where:

$$M_{1,\mathrm{Rd}} = \frac{f_{\mathrm{y}} t^2}{4} \text{ and } F_{2,\mathrm{Rd}} = f_{\mathrm{y}} t \tag{G2}$$

and differentiating to find the minimum value:

$$\frac{dF}{dl} = -\frac{4 M_{1,\mathrm{Rd}}}{l^2} + \frac{F_{2,\mathrm{Rd}}}{r} = 0 \tag{G3}$$

we determine the spacing as:

$$l = \sqrt{\frac{4M_{1,\mathrm{Rd}}r}{F_{2,\mathrm{Rd}}}} = \sqrt{rt} \tag{G4}$$

Hence by substituting in Equation (G1) the collapse line load is:

$$F = 2f_{\mathrm{y}}\sqrt{\frac{t^3}{r}} \tag{G5}$$

For a band-loaded long cylinder under a uniform area load of f over a band width b where $F = bf$ per unit circumferential length the equations become:

$$F\frac{\left(l - \frac{b}{4}\right)}{l}\delta = 4M_{1,\mathrm{Rd}}\frac{\delta}{l} + F_{2,\mathrm{Rd}}l\frac{\delta}{r} \tag{G6}$$

and differentiating to find the minimum value:

$$\frac{dF}{dl} = -\frac{4M_{1,\mathrm{Rd}}}{\left(l - \frac{b}{4}\right)^2} - \frac{F_{2,\mathrm{Rd}}l^2}{r\left(l - \frac{b}{4}\right)^2} + \frac{2F_{2,\mathrm{Rd}}l}{r\left(l - \frac{b}{4}\right)} = 0 \tag{G7}$$

we determine the spacing as:

$$l = \frac{b + \sqrt{b^2 + 16rt}}{4} \tag{G8}$$

Hence by substituting in Equation (G6) the collapse line load is:

$$F = 2lf_{\mathrm{y}}\frac{t}{r} \tag{G9}$$

Appendix H

Circular Plate

The failure load of a circular plate subjected to uniformly distributed load p, having radius r and thickness t, hinged or fixed at the edge has been cited in [21]. For a circular plate hinged at the edge $k = 3$, and built in at the edge $k = 5.364$, the solution obtained is:

$$p = \frac{kf_{\mathrm{y}}t^2}{2r^2} \tag{H1}$$

Appendix I

Spherical Cap

The failure load of a spherical cap subjected to radial uniformly distributed load p, having radius r and thickness t, and subtending a cap angle of 2α, hinged or fixed at the edge has been obtained by Hodge [35] and cited in [21]. For a spherical cap hinged at the edge the solution obtained is:

$$p = \frac{f_{\mathrm{y}}t}{r}\left[2 + \frac{t}{2r}\sin\alpha\left(\ln\frac{1+\sin\alpha}{\cos\alpha} - \sin\alpha\right)^{-1}\right] \tag{I1}$$

For a spherical cap built in at the edge the solution is obtained by solving two system of equations with an additional unknown quantity ϕ_1:

$$p = \frac{f_{\mathrm{y}}t}{r}\left[2 + \frac{t}{2r}\sin\phi_1\left(\ln\frac{1+\sin\phi_1}{\cos\phi_1} - \sin\phi_1\right)^{-1}\right] = \frac{f_{\mathrm{y}}t}{r}\left[2 + \frac{t}{2r}\left(\frac{1 + \ln\frac{\sin\alpha}{\sin\phi_1}}{\ln\frac{\cos\phi_1}{\cos\alpha}}\right)\right] \tag{I2}$$

Appendix J

Plate Without or With Holes or Notches Under Tension

The in-plane failure load based on direct tension failure $F_{\mathrm{t},1}$ or direct shear failure $F_{\mathrm{t},2}$ for a plate under tension with dimensions length l, breadth b, thickness t have been obtained in [26];

Plain plate:

$$F_{\mathrm{t},1} = f_{\mathrm{y}}bt, \quad F_{\mathrm{t},2} = \frac{2\tau_{\mathrm{y}}bt}{\sin 2\alpha} \text{ with } \alpha = 45^{o} \tag{J1}$$

Plate with hole with diameter d:

$$F_{t,1} = f_y(b - d)t, \quad F_{t,2} = \frac{2\tau_y(b - d)t}{\sin 2\alpha} \text{ with } \alpha = 45^o \tag{J2}$$

Plate with two notches with diameter d:

$$F_{t,1} = f_y(b - d)t, \quad F_{t,2} = \tau_y t \frac{b(2 + \cos 2\alpha_1 + \cos 2\alpha_2) - d(1 + 22\cos\alpha_2)}{2\sin(\alpha_1 + \alpha_2)\cos\alpha_1\cos\alpha_2} \text{ with } \alpha_1 = 52^o \;\&\; \alpha_2 = 38^o \tag{J3}$$

Appendix K

Plates

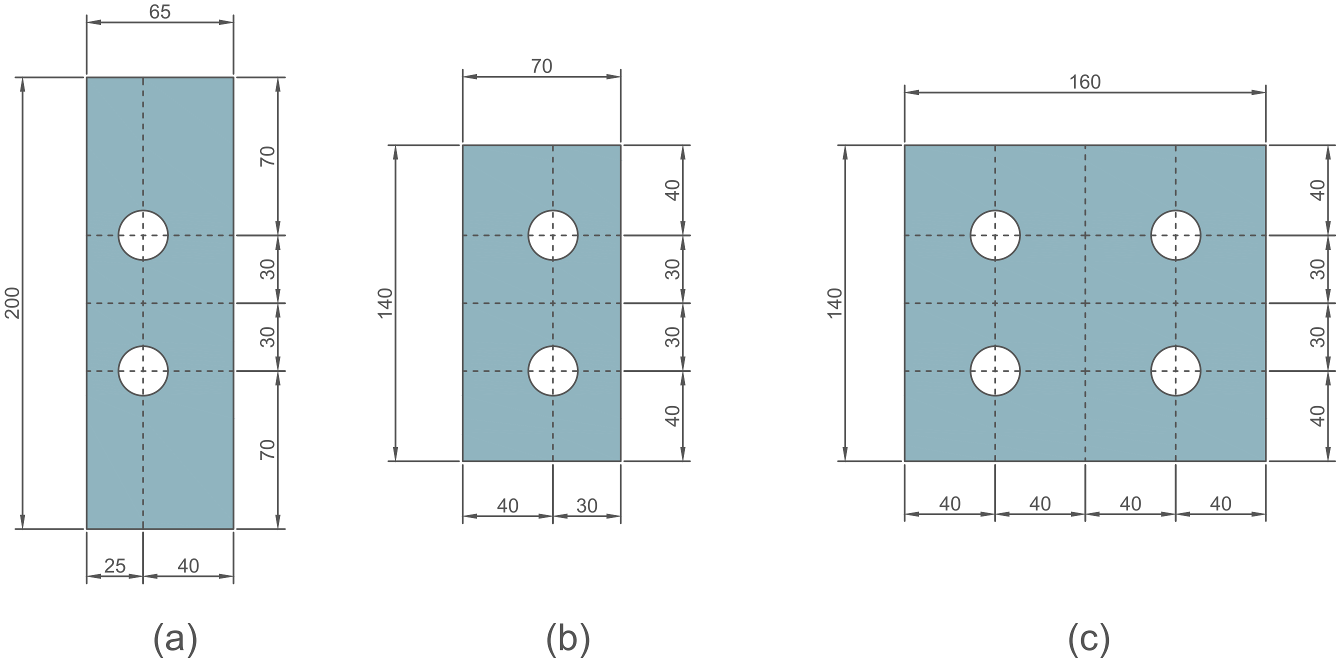

FIGURE K1 | Components of assembly: (a) notched web of beam; (b) fin plate of T-stub; (c) flange plate of T-stub.